

Kinetic Monte Carlo simulations of electrodeposition: Crossover from continuous to instantaneous homogeneous nucleation within Avrami's law

Stefan Frank^{a,b,c,1} Per Arne Rikvold^{a,b,c,d}

^a*Department of Physics, Florida State University, Tallahassee, FL 32306-4350, USA*

^b*Center for Materials Research and Technology, Florida State University, Tallahassee, FL 32306-4351, USA*

^c*School of Computational Science, Florida State University, Tallahassee FL 32306-4120, USA*

^d*National High Magnetic Field Laboratory, Tallahassee, FL 32310-3706, USA*

Abstract

The influence of lateral adsorbate diffusion on the dynamics of the first-order phase transition in a two-dimensional Ising lattice gas with attractive nearest-neighbor interactions is investigated by means of kinetic Monte Carlo simulations. For example, electrochemical underpotential deposition proceeds by this mechanism. One major difference from adsorption in vacuum surface science is that under control of the electrode potential and in the absence of mass-transport limitations, local adsorption equilibrium is approximately established. We analyze our results using the theory of Kolmogorov, Johnson and Mehl, and Avrami (KJMA), which we extend to an exponentially decaying nucleation rate. Such a decay may occur due to a suppression of nucleation around existing clusters in the presence of lateral adsorbate diffusion. Correlation functions prove the existence of such exclusion zones. By comparison with microscopic results for the nucleation rate I and the interface velocity of the growing clusters v , we can show that the KJMA theory yields the correct order of magnitude for Iv^2 . This is true even though the spatial correlations mediated by diffusion are neglected. The decaying nucleation rate causes a gradual crossover from continuous to instantaneous nucleation, which is complete when the decay of the nucleation rate is very fast on the time scale of the phase transformation. Hence, instantaneous nucleation can be homogeneous, producing negative minima in the two-point correlation functions. We also present in this paper an n -fold way Monte Carlo algorithm for a square lattice gas with adsorption/desorption and lateral diffusion.

Key words: kinetic Monte Carlo, Avrami's law, electrodeposition, underpotential

deposition, continuous nucleation, instantaneous nucleation, lattice-gas model, kinetic Ising model.

1 Introduction

The electrochemical adsorption of a two-dimensional film on a metal electrode can involve a phase transition at the surface [1]. When the adsorbate–adsorbate interactions are attractive, this phase transition is of first order; hence, below a critical temperature, there is a discontinuity in the coverage at a certain electrochemical potential. Stepping across the electrostatic potential difference between electrode and solution that corresponds to this coexistence point induces adsorption (or desorption). Whereas, thermodynamically, this phase transformation is abrupt rather than gradual, its kinetics are governed by the microscopic mechanism by which it proceeds. On a flat, defect-free single-crystal surface, the decay of the metastable phase takes place through nucleation and growth of two-dimensional clusters. The classical theory for this kind of phase change was developed in the 1930s and '40s by Kolmogorov, Johnson and Mehl, and Avrami (KJMA theory) [2–6]. Finding successful application in many fields of science, it is also the basis for the interpretation of kinetic data of electrodeposition processes that proceed by nucleation and growth [7, 8]. However, the assumptions of the theory may not always be met in real experimental systems. In particular, an earlier study from our group indicates that homogeneous nucleation can also be instantaneous, and that there might be a gradual crossover from continuous to instantaneous nucleation [9]. This casts some doubt on whether the nucleation is spatially uncorrelated [10, 11].

Lattice-gas models are now a widely applied tool in the study of electrochemical adsorption [12, 13]. They are appropriate when the adsorbate layer is commensurate with the substrate [14]. When the adsorbate is in quasi-equilibrium with the bulk under control of the electrode potential, a grand-canonical Hamiltonian should be used. Kinetic Monte Carlo simulations [15] of lattice-gas models can be used to study the dynamics of such systems when they can be well approximated as a superposition of independent, stochastic

Email addresses: stefan.frank@uni-ulm.de (Stefan Frank),
rikvold@scs.fsu.edu (Per Arne Rikvold).

URL: <http://www.physics.fsu.edu/users/rikvold/info/rikvold.htm> (Per Arne Rikvold).

¹ Present address: Zentrum für Sonnenenergie- und Wasserstoff-Forschung Baden-Württemberg, Helmholtzstraße 8, 89081 Ulm, Germany, and Universität Ulm, Abteilung Theoretische Chemie, 89069 Ulm, Germany.

processes [12]. This is generally true when the elementary processes evolve through thermally activated crossings of well-defined transition states. Then, one should choose an Arrhenius-type Monte Carlo dynamic [16, 17]. For the investigation of the model dynamics at macroscopic time scales this is the method of choice, since it does not rely on mathematical approximations and since it coarse-grains over the fluctuations (vibrations) whose time scales are orders of magnitude faster than adsorption, diffusion, etc. With this method real problems have been tackled and successfully described [18], for example for underpotential deposition of metals [19, 20]. However, the problem may require substantial effort in providing a sufficiently realistic description. For example, one may need to include coadsorption of anions, long-range or many-body potentials [14, 18, 21], etc.

Here we follow a somewhat different approach. Rather than in a specific system, we are interested in the general behavior of two-dimensional first-order phase transitions. Hence we choose as a model system a two-dimensional square lattice gas with nearest-neighbor attractive interactions. No solvent or counter ions are included. This model can be interpreted as a simplified description of electrochemical metal underpotential deposition or of the early stages of epitaxial growth when no nucleation takes place in the second layer. However, since it is isomorphic to the square-lattice Ising model [22], it is far more general and may, among other phenomena, also describe ferromagnetic systems [23]. The focus of this paper is on the influence of nearest-neighbor adsorbate diffusion on the dynamics of the phase transformation. Unlike in vacuum surface science, adsorbate diffusion is not a condition for nucleation since fluctuations in cluster sizes can also be mediated by the quasi-equilibrium with the solution (instead of the two-dimensional gas of adsorbed particles). Likewise, an earlier study [23] has shown that the phase-transformation dynamics of this lattice gas can be well described by the KJMA theory for continuous nucleation over a wide range of potentials in the *absence* of adsorbate diffusion (in magnetic terms, spin flip only). Another preliminary study [9] suggests that in the *presence* of diffusion (spin exchange in magnetic language) the dynamics may change. For fast diffusion, the phase transformation appeared to proceed by instantaneous nucleation, and for intermediate diffusion rates there was a gradual crossover. This was interpreted as a result of exclusion zones around the clusters, in which nucleation was suppressed. It was speculated that these exclusion zones may become space-filling in the early stages of the phase transformation. The crossover also changed the morphology of the adsorbate phase. However, the study used Glauber instead of Arrhenius dynamics and was limited to one value of the electrochemical potential. Here we extend the study to a wide range of potentials. Furthermore, we present a more stringent analysis of the kinetic data and use microscopic details of the simulation for comparison with the theory.

The remainder of this paper is organized as follows. In Sec. 2 we review the

KJMA theory and extend it to an exponentially decaying nucleation rate. In Sec. 3 we introduce the lattice-gas model and the details of the algorithm and the model calculations. Results are presented thereafter. In Sec. 4.1 we describe the phase transformation dynamics and the morphology of the adsorbate phase and give kinetic parameters according to the theory. In Sec. 4.2 we present the results for the microscopic rates. In Sec. 4.3 we discuss the accuracy of the continuum description of the KJMA theory, and in Sec. 4.4 we discuss under which conditions the crossover to instantaneous nucleation occurs. A summary and conclusions are given in Sec. 5. A description of the n -fold way algorithm for adsorption/desorption *and* diffusion can be found in the Appendix.

2 Theory

We here briefly review the KJMA theory and describe how we adapt it for a gradual crossover between continuous and instantaneous nucleation.

The basic assumption of the KJMA theory is that nucleation events are *random* and *uncorrelated*. Then, it is mathematically quite simple to correct for the overlap of growing circular droplets, provided that they do not change shape upon coalescence [24, 25]. One defines an *extended coverage* θ_{ext} by summing up the areas of all growing droplets regardless of overlap with other clusters, and normalizes this by the total surface area. When the radius r of a cluster is a function of its birth time \tilde{t} , this reads

$$\theta_{\text{ext}} = \int_0^{r_{\text{max}}} \rho(r) \pi r^2 dr = \pi v^2 \int_0^t I(\tilde{t}) (t - \tilde{t})^2 d\tilde{t}, \quad (1)$$

where $\rho(r)$ is the number of clusters of radius r per surface area, and $I(t)$ is the nucleation rate at time t . The last equality is for circular clusters with a radius growing linearly with an interface velocity v . It is important to realize that this nucleation rate includes nucleation events in the transformed area, since otherwise the condition of random, uncorrelated nucleation would be violated [26, 27]. There has been some confusion concerning this point [28]. We therefore call the nucleation rate $I(t)$ the *extended nucleation rate* wherever the distinction is important. In the system we consider in our investigation, nucleation is homogeneous and proceeds by thermal fluctuations. It can be described by classical nucleation theory [22], but we do not address this question further here.

When I is constant throughout the phase transformation, we speak of *continuous nucleation*, and performing the integration in Eq. (1) yields

$$\theta_{\text{ext}} = \frac{\pi I v^2 t^3}{3}. \quad (2)$$

Here, I has the dimension $1/(\text{area} \times \text{time})$. It is clear that the “real” nucleation rate I_r is reduced by the fraction of the covered surface θ and eventually decreases to zero; this is not to be confused with a decaying extended nucleation rate (see below). At early times, though, the real nucleation rate can be used as an estimate for the extended nucleation rate, since $\theta \approx 0$.

In contrast, when all nuclei are already present at the very beginning of the phase transformation and no further nucleation takes place, $I(t) = I\delta(t)$, where $\delta(t)$ is a Dirac delta function, and the integration in Eq. (1) yields

$$\theta_{\text{ext}} = \pi I v^2 t^2. \quad (3)$$

This *instantaneous nucleation* is often associated with heterogeneous nucleation at defects. Here, I has the dimension $1/\text{area}$ since it is virtually a surface density of nucleation centers.

The real coverage can be calculated from the extended coverage θ by [5]

$$1 - \theta = \phi_{\text{KJMA}} = e^{-\theta_{\text{ext}}}. \quad (4)$$

The quantity ϕ_{KJMA} is called the relaxation function (in the KJMA theory). We will later define a relaxation function for our model system and use ϕ_{KJMA} as a coarse-grained approximation for it [23].

2.1 Extended volume for decaying nucleation rate

The gradual crossover from continuous to instantaneous nucleation with increasing diffusion rate implies that, for some intermediate diffusion rates, the extended nucleation rate I is neither a constant nor a delta function, but decays with time. In the following, we deduce how an exponentially decaying extended nucleation rate

$$I(t) = I_0 e^{-\lambda t} \quad (5)$$

with I_0 the initial nucleation rate and λ an inverse decay time translates into a $\theta(t)$ relation for the coverage. The dimension of I_0 is $1/(\text{area} \times \text{time})$.

In Eq. (5), $I(t)$ is independent of the position. This is a mean-field approximation, in which any local reduction of the nucleation rate is smeared out over the whole surface. Within this approximation, nucleation remains spatially uncorrelated, and Avrami’s law [Eq. (4)] holds. Hence we need to calculate the extended coverage that follows from Eq. (5). Inserting $I(t)$ into Eq. (1) and performing the integration yields

$$\theta_{\text{ext}}(t) = \frac{\pi I_0 v^2 t^2}{\lambda} - \frac{2\pi I_0 v^2 t}{\lambda^2} + \frac{2\pi I_0 v^2}{\lambda^3} (1 - e^{-\lambda t}). \quad (6)$$

In the limit of $\lambda t \gg 1$, the second and the third term are of the order of λt and $\lambda^2 t^2$ smaller than the first term, and we recover the well-known result for instantaneous nucleation, Eq. (3), with $I = I_0/\lambda$. In the limit $\lambda t \ll 1$, the exponential can be expanded up to third order, which is the lowest non-vanishing order, and we recover the well-known result for continuous nucleation, Eq. (2), with $I = I_0$.

We note that the exponential decay of the extended nucleation rate is not derived from a physical model, but rather simply a mathematically convenient assumption. Moreover, in real systems as well as in our microscopic model system, the reduction of the nucleation rate is thought to be *local* in exclusion zones around existing clusters. This would violate the assumption that nucleation events are uncorrelated. Such correlations are ignored by the theory presented. A theory that includes these effects could not make use of Avrami's law.

A fit of experimental or simulation results for the relaxation function to Eqs. (4) and (6) can yield estimates for λ and for $I_0 v^2$, but no separate estimates for I_0 and v .

3 Model and algorithm

3.1 Model

We model the electrodeposition process using a square lattice-gas model with attractive nearest-neighbor interactions. Since the subcritical fluctuations of the adsorbate are at quasi-equilibrium, a grand-canonical Hamiltonian is used:

$$\mathcal{H} = -\Phi \sum_{\langle i,j \rangle} c_i(t)c_j(t) - \mu \sum_i c_i(t), \quad (7)$$

where Φ is the lateral interaction constant and μ the electrochemical potential of the adsorbing ion in the solution². Mass-transfer limitations from the solution to the surface are neglected. The occupation variables c_i take the value 0 when site i is empty, and 1 when it is occupied.

We perform simulations for an $L \times L = 256 \times 256$ lattice with periodic boundary conditions, using for all simulations the interaction constant $\Phi = 4$ and the

² For a spin $s_i = \pm 1$ Ising model with z nearest neighbors (here, $z = 4$) and \mathcal{N} sites, coupling constant J and external magnetic field H , the mapping between the models is $\mathcal{H}_I = \mathcal{H}_{LG} + (\mathcal{N}/2) [\mu - (\mu_0/2)]$, $c_i = (s_i + 1)/2$, $\Phi = 4J$, $\mu - \mu_0 = 2H$, and $\mu_0 = -2zJ$ [22].

temperature $T = 0.8 T_c \approx 0.454 \Phi = 1.815$, where T_c is the critical temperature of the Ising model for the given parameters [29]. Energy and temperature units are chosen such that Boltzmann's constant $k_B = 1$.

3.2 Algorithm

The dynamics of the phase transformation are investigated using kinetic Monte Carlo simulations [15]. We assume that the model dynamics can be reasonably approximated by a few stochastic elementary processes; hence, we choose one-step Arrhenius-type dynamics [16, 17] for the transition probabilities, introducing a local transition barrier Δ . The transition rate R for a transition from configuration a to configuration b is approximated by the corresponding rate for a transition from a to a fictitious transition state:

$$R(a \rightarrow b) = \nu_0 \exp\left(-\frac{\mathcal{H}^\dagger - \mathcal{H}(a)}{k_B T}\right), \quad (8)$$

where \mathcal{H}^\dagger is the energy at the transition state. Using a symmetric ($\alpha = 1/2$) Butler-Volmer- (Brønsted-)type expression for \mathcal{H}^\dagger [12]:

$$\mathcal{H}^\dagger = \frac{\mathcal{H}(a) + \mathcal{H}(b)}{2} + \Delta, \quad (9)$$

one obtains

$$R(a \rightarrow b) = \nu_0 \exp\left(-\frac{\Delta}{k_B T}\right) \exp\left(-\frac{\mathcal{H}(b) - \mathcal{H}(a)}{2k_B T}\right), \quad (10)$$

where ν_0 sets the Monte Carlo time scale and will be chosen as unity in the following. Another choice for an Arrhenius-type dynamic is the transition-dynamic algorithm [30, 31].

For each kind of elementary step that is included in our model simulations, we specify a value for the transition barrier Δ . In particular, these are $\Delta_{\text{ad/des}}$ for adsorption/desorption steps and Δ_{dif} for diffusion steps to a nearest-neighbor site. The former is equivalent to a spin-flip step, the latter to a spin-exchange step in the terminology of magnetic spin models. By varying the difference $\Delta_{\text{ad/des}} - \Delta_{\text{dif}}$ we can set the ratio between adsorption/desorption and diffusion steps. The absolute values have no particular meaning unless we attempt to specify the relation between physical and Monte Carlo time scales [18]. We treat Δ as merely formal and note that, according to Eq. (9), \mathcal{H}^\dagger might not be larger than both $\mathcal{H}(a)$ and $\mathcal{H}(b)$ for a strongly exothermic or endothermic step, viz not represent a true barrier, even for positive Δ . In the Monte Carlo algorithm chosen, transition rates $R > 1$ pose no problem (see below).

At high diffusion rates, standard Monte Carlo algorithms are prohibitively slow since much simulation time is spent on the coverage-conserving diffusion steps. It is therefore necessary to use more advanced methods: we choose the n -fold way algorithm of Bortz, Kalos and Lebowitz [32] and Gilmer [33]. This algorithm is rejection-free: of all possible new configurations, one is chosen with probability R_j/R_{tot} , where $R_{\text{tot}} = \sum_i R_i$, and then accepted with probability 1. No time is spent on choosing sites and calculating energy differences for rejected moves. After each step the simulation time is updated by $-(1/R_{\text{tot}}) \ln r$ MCSS (Monte Carlo steps per site), where r is drawn from a uniform pseudo-random distribution between 0 and 1. We need to keep a list of the transition rates for all possible moves from the actual configuration. This is done for a single-site n -fold way as follows. For each site s in the lattice we compute the transition rate $R_{s,m}$ for every possible elementary step m according to Eq. (10): adsorption/desorption ($R_{s,1}$; adsorption when site is empty, desorption otherwise); exchange with nearest neighbor to the right ($R_{s,2}$; equal to zero when both are occupied or both are empty), exchange with nearest neighbor below ($R_{s,3}$; equal to zero when both are occupied or both are empty). This minimizes the possible steps per site and makes sure that every possible diffusion step on the lattice is counted once. We then calculate the total rate at which site s performs a move as $S_s = \sum_m R_{s,m}$. In a Monte Carlo step, a random number is drawn from a uniform distribution to choose with probability S_s/R_{tot} the site s that performs the next move. Then, another random number is drawn to choose with probability $R_{s,m}/S_s$ which elementary step m is performed. Finally, a third random number is drawn to choose the time step by which the simulation clock is updated. After that, the respective R and S of all sites that are affected by the move are updated. In order to accelerate this process, the latter are stored in a binary tree.

Recognizing that there is a finite number of configurations of a site plus environment, each characterized by an energy that is constant throughout the simulation, it is in principle possible to tabulate the energy differences that are connected with each change of local configuration (called classes). This has previously been worked out for the square Ising lattice without spin-exchange (diffusion) [32], where 10 classes are to be considered for adsorption/desorption. Here, we additionally have to define 32 classes for the diffusion step; our n -fold way is hence a 42-fold way algorithm. The situation is further complicated by the fact that the diffusion step calls for including a larger portion of the lattice into the affected environment of a site. We have to consider a total of 21 classes up to third-nearest neighbor positions after an adsorption/desorption step and of 31 classes up to fourth-nearest neighbor positions after a diffusion step. Details are shown in the Appendix.

3.3 Model calculations

Our goal is the investigation of the influence of diffusion on the dynamics of the first-order phase transition. To that end, we vary the diffusion barrier Δ_{dif} between 5 and 15, keeping $\Delta_{\text{ad/des}} = 15$ constant. Moreover, we perform simulations without diffusion, corresponding to $\Delta_{\text{dif}} = \infty$. We start our simulations with an empty lattice, and at $t = 0$ we set the electrochemical potential to a value between $\mu - \mu_0 = 0.4$ and $\mu - \mu_0 = 1.6$, where μ_0 is the electrochemical potential at coexistence. For all these values of the electrochemical potential, the phase transformation is in the multi-droplet regime [23], where the number of supercritical adsorbate clusters is large. For each set of parameters, we perform 500 to 1000 independent simulation runs. This high number is necessary to accurately obtain the variance of the coverage. For quantities that do not depend on higher moments, we typically take statistics from only about 100 runs.

We sample the coverage θ as a function of the simulation time. Moreover, we follow the size of every cluster in the lattice throughout the simulation until the coverage reaches $\theta = 1/2$; this enables us to get microscopic interface velocities and nucleation rates. Later, cluster sizes are obtained using the Hoshen-Kopelman algorithm [34] at certain coverages. We compute the time-dependent two-point correlation function (see Ref. [23], correcting for missing factors of powers of L)

$$G(\vec{r}, t) = \langle c_i(t)c_j(t) \rangle - \langle \theta(t) \rangle^2, \quad (11)$$

where $\vec{r} = \vec{r}_i - \vec{r}_j$, as $1/\sqrt{L^2}$ times the inverse Fourier transform of the structure factor

$$S(\vec{q}, t) = \langle \hat{c}_{\vec{q}} \hat{c}_{-\vec{q}} \rangle - L^2 \langle \theta(t) \rangle^2 \delta_{\vec{q}, \vec{0}}, \quad (12)$$

where $\delta_{\vec{q}, \vec{0}}$ is the Kronecker delta function and $\hat{c}_{\vec{q}}$ is the Fourier transform of c_i :

$$\hat{c}_{\vec{q}}(t) = \frac{1}{\sqrt{L^2}} \sum_{i=1}^{L^2} c_i(t) \exp(-i\vec{q} \cdot \vec{r}_i). \quad (13)$$

The angular brackets denote averages over independent runs. Due to the use of a Fast Fourier Transform algorithm [35], this approach is significantly faster than the direct calculation of $G(\vec{r}, t)$. We only report the circularly averaged $G(r, t)$.

4 Results

Our interest is in the influence of diffusion on the kinetics and dynamics of the phase transformation. It is therefore necessary to first characterize how

the fraction of steps that are diffusion steps depends on the model parameters. We count the diffusion steps and divide their number by the number of total steps. Since the time step by which the clock is updated after a successful move does not depend systematically on the type of move performed, this simpler approach is approximately equivalent to computing true rates of the elementary processes. Figure 1 shows that the fraction of diffusion steps changes only weakly during the phase transformation. Hence, it is sufficient to discuss the average fraction of diffusion steps throughout the whole simulation. In Table 1, we show that the diffusion fraction increases strongly with decreasing diffusion barrier Δ_{dif} , reflecting the exponential law, Eq. (10), and increases weakly with the electrochemical potential, reflecting that diffusing particles spend on average longer time on the surface before they desorb. With $\Delta_{\text{dif}} = 5$, diffusion is the predominant process.

The critical cluster size n^* is governed by the balance of volume and surface free-energy terms of the clusters [22, 36]; it hence depends on the interaction constant Φ (which we keep constant), and on the electrochemical potential μ (which we vary). The critical cluster size is the number of particles n in the cluster for which the free energy $F(n)$ has a maximum. We calculate $F(n) = -k_{\text{B}}T \ln Z(n)$ from the restricted partition function $Z(n)$, which we obtain from enumerating lattice animals, hence counting all possible configurations of a given cluster size [9]. The resulting critical cluster size is shown as a function of μ in Table 2. As expected, it decreases with increasing μ .

4.1 Dynamics of the phase transformation

We characterize the phase transformation using the relaxation function ϕ [23], which is closely related to $1 - \theta$ and decays from 1 to 0 during the adsorption. It is defined as

$$\phi(t) = \frac{\theta(t) - \theta_{\text{s}}}{\theta(0) - \theta_{\text{s}}}, \quad (14)$$

where θ_{s} is the stable coverage, which depends on the electrochemical potential and is easily obtained from equilibrium Monte Carlo simulations. We define the metastable lifetime τ as the time when $\phi = 1/2$.

The influence of the electrochemical potential on the kinetics of the phase transformation is shown in Fig. 2. The phase transformation lags behind the potential switch, but it is markedly accelerated when the electrochemical potential, which is the driving force for adsorption, is higher. In Fig. 3 we show the influence of diffusion on the kinetics for $\mu - \mu_0 = 0.4$. At $\Delta_{\text{dif}} = 15$, the phase transformation is only slightly faster than in the absence of diffusion; however, at lower values of the diffusion barrier, the acceleration is considerable. This trend is verified in Table 3 for all electrochemical potentials and diffusion barriers considered.

In a previous investigation [9], using Glauber dynamics, we found that when diffusion is sufficiently fast on the time scale of adsorption/desorption, there is a crossover from continuous to instantaneous nucleation. We demonstrate in Fig. 4 that this behavior persists when introducing local barriers into the dynamics. We normalize the time scale with the metastable lifetime; then, when only the time scale of the phase transformation changes and not the dynamics, the plots should collapse. This is the case for the simulations without diffusion and with $\Delta_{\text{dif}} = 15$, but for lower diffusion barriers we find increasingly strong deviations. Figure 4(a) shows the plot for the model of continuous nucleation [Eqs. (2) and (4)]. The deviations from linearity at early times probably come from an overlap of the time scales of the formation of the metastable phase (starting with a completely free surface) and of the metastable decay. However, in the absence of diffusion, there is a marked region where linear behavior is found. This region becomes shorter and eventually disappears when diffusion becomes predominant. Instead, as shown in Fig. 4(b), for $\Delta_{\text{dif}} = 5$ the prediction for instantaneous nucleation [Eqs. (3) and (4)] is fulfilled. Similar results were reported in Ref. [9].

4.1.1 Crossover to instantaneous nucleation

On the basis of the results from the previous section, we attempt to fit the phase transformation curves to our model for decaying nucleation rates (Sec. 2.1). According to Ref. [23], when the KJMA theory is used as a coarse-grained approximation for the microscopic Ising (or lattice-gas) model, the relaxation function can be corrected for the fact that the simulation does not start from the metastable phase:

$$\phi(t) \approx \frac{\theta_{\text{ms}} - \theta_{\text{s}}}{\theta(0) - \theta_{\text{s}}} \phi_{\text{KJMA}}(t). \quad (15)$$

In a first step, we fit $\phi(t)$ from the simulations without diffusion to Eqs. (2), (4), and (15) and obtain estimates for the two free parameters of the fit, Iv^2 and θ_{ms} . To do so, we need an estimate for θ_{s} , which we obtain from equilibrium Metropolis Monte Carlo simulations of the order of 10^6 MCSS. The thermodynamic quantity θ_{ms} is only a function of T and μ and independent of the microscopic details of the dynamics. It can therefore be used later for the simulations with diffusion at the same potential. Strictly, due to the imperfect separation of the timescales for the metastable decay and the formation of the metastable phase from the empty surface, the estimates for θ_{ms} obtained in this way are compromised by a systematic error. In particular at higher potentials they appear to be too high, and we refrain from reporting their numerical values. However, the error is most likely dominated by the potential and not by the diffusion rate, and we use the same θ_{ms} for all diffusion rates at the same potential in the following.

In a second step we fit $\phi(t)$ from all the simulations (with and without diffusion) to Eqs. (4), (6), and (15). The free parameters of the fit are I_0v^2 and λ . The former contains information about the kinetics of the phase transformation, the latter about the decay time of the nucleation, viz the dynamics of the phase transformation. We fit the relaxation function in the interval from 0.5τ to τ , since at short times the decay to the metastable phase affects ϕ , and at longer times coalescence effects become noticeable [9]. By dividing the data into about 10 to 20 subsets and performing the fit independently for each subset, we obtain the standard deviation of the fitting parameters, and hence an estimate of the standard error.

In Table 4 we show the results for the kinetic parameter I_0v^2 . The standard error is insignificant for the number of digits given. The values of Iv^2 reflect the same trends as the metastable lifetime τ . In the absence of diffusion and for $\Delta_{\text{dif}} = 15$, the values are identical to those obtained for Iv^2 from fits to Avrami's law for continuous nucleation. For the values for which we expect a possible crossover to instantaneous nucleation to be most complete ($\mu - \mu_0 = 1.6$, $\Delta_{\text{dif}} = 5$) $I_0v^2/\lambda = 1.3 \times 10^{-9}$, in satisfactory agreement with $Iv^2 = 9.5 \times 10^{-10}$ from a fit to Avrami's law for instantaneous nucleation.

This behavior is reflected in the values of $\lambda\tau$ that we report in Table 5. When $\lambda\tau = 1$, the nucleation rate has decayed by a factor $1/e$ at the metastable lifetime. Hence, when $\lambda\tau \approx 1$, we are in a transition regime where the Avrami plots neither resemble instantaneous nor continuous nucleation. In the regime of continuous nucleation, $\lambda\tau \ll 1$; the exact numerical value is insignificant and thus scatters. This can cause quite large relative standard errors. When $\lambda\tau$ becomes larger, we are approaching the regime of instantaneous nucleation. These finite values of $\lambda\tau$ are indeed significant, as shown by the quite small statistical errors in these cases. As the results in the previous paragraph suggest, for the highest potential and lowest diffusion barrier considered, the nucleation is virtually instantaneous. A value of $\lambda\tau \approx 4$ means that the extended nucleation rate I is reduced to about $I_0/50$ when the relaxation function reaches $1/2$. We show the fits for $\mu - \mu_0 = 1.2$ in Fig. 5 to demonstrate how the model captures the crossover from continuous to instantaneous nucleation. Apart from deviations at early times, the fits are satisfactory. The decrease in curvature with increasing diffusion rates is well captured.

4.1.2 Morphological changes

In Ref. [9] we demonstrated that the crossover from continuous to instantaneous nucleation is accompanied by changes in the adsorbate morphology during the phase transformation. In particular, the cluster-size distributions showed a depletion of mid-sized clusters and an enrichment of large clusters. Here we show that similar behavior is found using dynamics with local barri-

ers.

According to Sekimoto’s theory for uncorrelated, continuous nucleation [37, 38], the two-point correlation function $G(r)$ is a monotonically decreasing function of the distance r . We show the results for $\mu - \mu_0 = 0.4$ and $\Delta_{\text{dif}} = \infty$ in Fig. 6 (a). The correlation functions indeed decay monotonically for all coverages. As can be easily shown from the definition of $G(r)$, $G(0) = \langle \theta \rangle - \langle \theta \rangle^2 = \langle \theta \rangle (1 - \langle \theta \rangle)$, which equals the mean-square fluctuation of the occupation variable from its average [39]. For later use, it is convenient to normalize the correlation function as $\tilde{G}(r) = G(r)/G(0)$, such that $\tilde{G}(0) = 1$. The un-normalized $G(0)$ assumes the same value for coverages that add up to 1, and is maximal for $\theta = 0.5$. The high-coverage correlation function of these pairs always decays more slowly, showing the asymmetry of the morphology about $\theta = 0.5$. It has been shown in Ref. [23] that the agreement of Sekimoto’s theory with $G(r)$ is very good in the absence of diffusion. Only at short length scales are there some deviations due to the in-phase correlations which are neglected in the theory. The effect of diffusion on $G(r)$ is shown in Fig. 6 (b). Here, for $\mu - \mu_0 = 1.6$ and $\Delta_{\text{dif}} = 5$, the correlation function decays to negative values, and after going through a minimum converges to 0. The negative values of $G(r)$ reflect the exclusion zones around existing clusters, in which nucleation is diminished since aggregation to the cluster is more likely than the formation of a new cluster. This result is very important since it shows a violation of the assumptions behind the KJMA theory and makes the use of Avrami’s law in the interpretation of the phase-transformation kinetics questionable. Any quantitative errors of the nucleation rate and interface velocity estimated on the basis of the KJMA theory are most likely due to these diffusion-induced correlations. We note that similar minima are also found in the two-point correlation functions during phase separation with a conserved order parameter [40], but not during phase ordering with a non-conserved order parameter. As in the case studied here, negative correlations during phase separation are mediated by diffusion. In our simulations, the minima occur first when $\lambda\tau$ is of the order of 1 (see Section 4.1.1). They are most pronounced around $\theta = 0.5$. With increasing coverage they move toward larger r since the average cluster size increases.

From the inverse of the initial slope of the normalized correlation function $\tilde{G}(r)$ we can estimate the correlation length l . As we show in Fig. 7, the correlation length as a function of the coverage is a concave function with the maximum shifted to values larger than $\theta = 0.5$. This shows that correlations are of longer range for the vacancy clusters at coverage $1 - \theta$ than for the corresponding adatom clusters at coverage θ . Generally, the correlation length decreases with increasing μ , and increases with decreasing Δ_{dif} , indicating that diffusion causes the formation of larger structures on average. This is corroborated by an investigation of the cluster-size distributions. Figure 8 shows as a typical example the distributions for $\mu - \mu_0 = 1.6$ at $\theta = 0.3$.

With rapid diffusion, the densities for the largest clusters are enhanced at the expense of mid-sized clusters. Similar results were found in Ref. [9].

Some of these observations can easily be verified from inspecting snapshots of the real-space morphology, like the ones shown in Fig. 9. The asymmetry of the morphology about $\theta = 0.5$ is clearly visible comparing the snapshots at $\theta = 0.3$ and $\theta = 0.7$ for all potentials and diffusion barriers shown. There are fewer, but larger vacancy islands at the higher coverage than adsorbate islands at the lower coverage, and their shape is markedly more different from circular. The average island size at the same coverage increases with decreasing potential and with increasing diffusion rate, causing the observed trends for the correlation length.

4.1.3 Separate nucleation rate and interface velocity

Within the KJMA theory for spatially random, continuous nucleation, Sekimoto [37, 38] has derived an expression for the two-point correlation function $\Gamma(r)$ as a function of the nucleation rate, the interface velocity, and time. $\Gamma(r)$ can be used as a coarse-grained approximation for the correlation function $G(r)$ from our simulations. From Eqs. (12) and (13) it can be shown that

$$S(\vec{0}) = L^2 \text{var}(\theta) = \sum_i^{L^2} G(\vec{r}_i). \quad (16)$$

The last equality is the inverse Fourier transform for $\vec{q} = \vec{0}$. Hence, fitting the simulation results for $L^2 \text{var}(\theta)$ to Sekimoto's expression for Γ can yield separate estimates for the nucleation rate and the interface velocity I and v , respectively [23], provided the assumptions of Sekimoto's derivation hold. Taking into account the coarse graining and local fluctuations, one obtains [23]

$$L^2 \text{var}(\theta) \approx [\theta_{\text{ms}} - \theta_{\text{s}}]^2 8\pi v^2 t^2 \phi_{\text{KJMA}}^2 \times \left[\Theta(Iv^2 t^3) - \frac{1}{2} \right] + \phi_{\text{KJMA}} k_{\text{B}} T \chi_{\text{ms}} + [1 - \phi_{\text{KJMA}}] k_{\text{B}} T \chi_{\text{s}}. \quad (17)$$

The function

$$\Theta(x) = \int_0^1 y e^{x\Psi(y)} dy \quad (18)$$

is obtained by numerical integration using

$$\Psi(y) = \frac{2}{3} \left[\arccos(y) - 2y\sqrt{1-y^2} + y^3 \ln \left(\frac{1 + \sqrt{1-y^2}}{y} \right) \right]. \quad (19)$$

Here, χ_{s} and χ_{ms} describe the local fluctuations of the stable and the metastable phase, respectively. The former is equivalent to the susceptibility in magnetic language and can be obtained from equilibrium Monte Carlo simulations [41].

Iv^2 in the argument of Θ is known from the fits to Avrami’s law for decaying nucleation rate (Section 4.1.1). The free parameters of the fit are the interface velocity v and χ_{ms} . Knowledge of v and Iv^2 enables the calculation of I ; we do not report the results for χ_{ms} .

The model fits the data very well for low supersaturation and high diffusion barriers. The quality of the fits decreases a little with increasing supersaturation. For $\Delta_{\text{dif}} = 5$, though, Sekimoto’s model is not capable of describing the data. Obviously, diffusion causes a violation of its underlying assumptions. In particular, nucleation is no longer spatially random. We therefore exclude all simulations which show minima in the two-point correlation function $G(r)$ from this analysis. Results for the nucleation rate and the interface velocity are shown in Tables 6 and 7, respectively. The nucleation rate grows strongly with the supersaturation — by more than two orders of magnitude from $\mu - \mu_0 = 0.4$ to $\mu - \mu_0 = 1.6$. The interface velocity increases in the same sense, but less dramatically, by less than an order of magnitude. Due to the limitations of the model, no statement can be made about the trend with (noticeable) diffusion rates. Hence, and also for comparison with the data without diffusion, we will in the following use information from the microscopic details of the simulations.

4.2 Microscopic rates

To obtain microscopic nucleation rates and interface velocities, we follow the time development of the size (number of particles) n of every cluster during a simulation run. An adsorption step can cause the coalescence of two or more clusters. A desorption step can cause the dissociation of a cluster; one needs to check every time if the possible fragments are still connected. The algorithm can be accelerated by realizing that the maximum number of fragments is the number of nearest neighbors of the desorbed particle. Moreover, it is faster to look for connections in the vicinity of the desorbed particle first.

We count coalescence and dissociation events. The evaluation of nucleation events is described in Section 4.2.2. Diffusion is treated as an adsorption step followed by a desorption step. Beyond the percolation threshold the algorithm is prohibitively slow, and we use it only up to $\theta = 0.5$.

4.2.1 Interface velocity

The KJMA theory in the present form makes use of the common assumption that the radius of a circular cluster grows linearly with time (Allen-Cahn approximation [22, 37, 38]). This assumption is expected to be very good for cluster sizes much larger than the critical cluster, but it ignores effects of

the surface tension and of the local environment (the diffusion field). During the phase transformation of the (Ising) square lattice-gas model in the multi-droplet regime the clusters are not perfectly circular [9,23], but one can define an effective radius $r = \sqrt{n/\pi}$. We compute at t_1 the microscopic interface velocity for every supercritical cluster i which has been born at $t_{0,i}$, as $v_i = (r_i(t_1) - r_i(t_{0,i})) / (t_1 - t_{0,i})$, while excluding very recently nucleated clusters ($t_{0,i} \leq 0.75t_1$). Here, t_1 is the first time the coverage in the actual simulation runs reaches $\theta = 0.1$, thus minimizing the effect of coalescence (see below). The resulting distribution of microscopic interface velocities for each set of simulation parameters is roughly bell-shaped and yields the mean and standard deviations given in Table 7. The mean microscopic interface velocities increase somewhat with increasing supersaturation, and in quite a pronounced manner with the diffusion rate. Where data are available, the rates from Sekimoto's theory are in good agreement. The standard deviations are typically about half of the mean. For the simulations in the absence of diffusion, the interface velocity compares quite well with the results from a dynamic mean-field approximation for a solid-on-solid interface under the same microscopic dynamics [42]. This is also shown in Table 7.

4.2.2 Nucleation and coalescence rates

In classical nucleation theory, for a sufficiently low supersaturation and for a large critical nucleus, nucleation kinetics can be described by the Fokker-Planck equation, as the superposition of a drift and a diffusional motion in particle-size space [43]. The former is driven by the derivative of the cluster free energy $F(n)$ with respect to the cluster size n , and the latter is a stochastic fluctuation of the particle size.

A nucleation event happens when a cluster grows to a size larger than a certain cutoff n_c . Likewise, a supercritical cluster dissolves when it shrinks back to a size less than or equal to n_c . When one supercritical cluster splits into two supercritical clusters, this is not counted as nucleation, and when two supercritical clusters coalesce, this is not counted as dissolution of the vanishing cluster. At the top of the free-energy barrier, when $n_c = n^*$, these processes are dominated by the diffusional motion in n -space. Far away from the barrier, this diffusional motion can be neglected. The diffusion length in n -space is [43]

$$l_n = \left(\frac{D}{-\left(\frac{d^2F(n)}{dn^2}\right)_{n=n^*}} \right)^{1/2}, \quad (20)$$

where $D = k_B T$ and $F(n)$ is the free energy of a cluster of size n . From a parabolic fit of the barrier region of $F(n)$ for $\mu - \mu_0 = 0.4$ this yields $l_n = 11$. In Fig. 10 we compare the raw nucleation and dissolution rates for $n_c = n^* = 18$ and for $n_c = n^* + l_n = 29$. The difference between the raw

nucleation and dissolution rates yields the net nucleation rate. Choosing the larger cutoff, the diffusional motion is somewhat reduced, but not eliminated, and the net nucleation rate takes longer to reach its plateau value. We thus use $n_c = n^*$ in the following. We further note that the conditions for the validity of a Fokker-Planck equation are not strictly fulfilled with the model parameters used.

The nucleation rates obtained with this method are real nucleation rates, I_r . Figure 11 shows the net nucleation rate for $\mu - \mu_0 = 1.2$ in the absence of diffusion and for fast diffusion rates. In both cases the net real nucleation rate rises steeply in the initial phase and goes through a maximum; it then decreases continuously to zero. We show this for all diffusion rates investigated at this supersaturation in Fig. 12, where the time scale is normalized to the metastable lifetime, separating changes in the dynamics from a mere acceleration of the phase transformation. The decrease is much faster when diffusion rates are high. This gives an *a posteriori* justification for using a decaying extended nucleation rate in the analysis of the relaxation function at least on a qualitative level. However, it is quite noticeable that even in the absence of diffusion the real nucleation rate reaches zero when only about half of the surface is covered. This is clearly in contradiction to the assumed constant extended nucleation rate in KJMA theory (which would result in a drop of the real nucleation rate to half its maximum value at this coverage).

Figure 11 also shows the net coalescence rate, which is the difference between the rates at which supercritical clusters vanish by coalescence and appear by dissociation. For fast diffusion rates it increases more strongly in the initial phase, but saturates earlier and at lower values than in the absence of diffusion. We show this for all diffusion rates investigated at this supersaturation in Fig. 13, where the time scale is normalized to the metastable lifetime. We believe that this pattern of the coalescence rate for fast diffusion is related to the changes in morphology (Section 4.1.2). The initially more effective coalescence results in a reduction of the density of mid-sized clusters and an increase of the correlation length, such that later on fewer clusters are prone to coalesce in the more strongly ordered adsorbate layer. The difference between the net nucleation and coalescence rates is the net rate at which supercritical clusters are formed. Its integral over time perfectly reproduces the time-dependent densities of supercritical clusters, corroborating the accuracy of our cluster-counting method and analysis.

In the absence of diffusion, the decrease of the real nucleation rate comes from the reduction of the free surface area. Its maximum value at low coverage thus gives an estimate of the extended nucleation rate I in the KJMA theory. The results are shown in Table 6. They are of the same order as the results from Sekimoto's theory, though systematically a little higher.

When the microscopic net nucleation rate reaches its maximum, the net coalescence rates are still close to zero. This implies that the real nucleation rates at early times so obtained should be a good estimate for the extended nucleation rate, since the microscopic nucleation rate is reasonably well separated from coalescence processes. Also, the microscopic nucleation rate should be very close to the time derivative of the density of supercritical clusters in the initial period of the phase transformation. This is indeed borne out by our results which are shown in Table 6.

4.2.2.1 Simulations of the metastable phase Further insight into the nature of the nucleation process is gained by simulations in which we suppress the decay of the metastable phase and the adsorption of supercritical clusters. We start the simulations with an empty surface and at time $t = 0$ we switch on a supersaturation favorable for adsorption. We follow the sizes of all clusters at every Monte Carlo step. Whenever a step produces a supercritical cluster, this whole cluster is desorbed and the event counted as a nucleation event. The histogram for the time between two nucleation events, t_{nucl} , is shown in Fig. 14 as a log-lin plot for $\mu - \mu_0 = 1.2$; the plots for the other supersaturations look similar. The probability distribution of t_{nucl} decays exponentially, as expected for a Poisson process. A further indication is the fact that the standard deviation of t_{nucl} equals its mean $\langle t_{\text{nucl}} \rangle$ (see Table 6). It must be noted that, since there are never any stable clusters present on the surface the effects of spatial correlation on the nucleation rate are neglected. The nucleation rates obtained from the reciprocal of $L^2 \langle t_{\text{nucl}} \rangle$ are about a factor two larger than the microscopic rates obtained from the simulations of the phase transformation. This corresponds to a transmission factor of about 1/2 for the diffusional motion across the nucleation barrier in n -space. For fast diffusion rates the discrepancy is a little larger, which might be an effect of the absence of exclusion zones in which no nucleation can take place in these “simulations of the metastable phase”. We emphasize that no real metastable phase is produced by this method since the complete desorption of supercritical clusters disturbs the quasi-equilibrium.

4.3 Accuracy of the continuum description

The time-dependent law for the extended nucleation rate that we used for the analysis of the phase-transformation dynamics is a mean-field approximation whose accuracy is difficult to predict (see Section 2.1). Our simulations have shown a strong decrease of the real nucleation rates in the presence of fast diffusion. However, not even in the absence of diffusion does the real nucleation rate follow exactly the assumptions of the theory (Section 4.2.2). Moreover, the two-point correlation functions of the adsorbate phase indicate

that the condition of spatially random nucleation is violated when diffusion rates become noticeable (Section 4.1.2). A check of the validity of Avrami's law applying an exponentially decaying extended nucleation rate to describe the phase transformation in the present microscopic model, is to compare the kinetic parameter Iv_{model}^2 from the fit of the relaxation function to the theory with Iv_{micro}^2 calculated from the microscopic rates I and v . We assume here that the latter represents the correct value. This is shown in Fig. 15.

In the absence of diffusion and for low diffusion rates the agreement is very good. When the diffusion rate increases, we find systematic deviations: the result from the fit is increasingly too low. Still the fits yield the correct order of magnitude for Iv^2 . Hence, the agreement between the KJMA theory for exponentially decaying nucleation rates and the microscopic results is quite satisfactory, keeping in mind that the former is only a coarse-grained continuum approximation of our microscopic model system. In particular, the incomplete separation of the time scales for the formation and the decay of the metastable phase is a potential source for deviations and limits the quality of the curve fitting. Introducing an additional fitting parameter that shifts the time scale might improve the ability of the model to fit the shape of the phase-transformation curves, but its physical meaning would be questionable.

In the limit of instantaneous nucleation, I_0/λ should equal the density of nuclei. This can be checked using the microscopic I_r at early times as an estimate for I_0 and the maximum density of supercritical clusters as an estimate for the density of nuclei. The results are presented in Table 8. They show quite good agreement and the correct trend with the supersaturation, despite the deviations of Iv^2 under the respective conditions. Hence, λ is indeed physically meaningful and not a mere model parameter.

We point out that the presented theory does not account for spatial correlations between the nuclei that are a consequence of the diffusion-induced exclusion zones. It is difficult to anticipate the consequences of an appropriate extension of the theory. However, since these correlations shift the overlap between growing extended clusters to later times, accelerating the phase transformation at early times, one might speculate that the discrepancies in Iv^2 would rather increase. We conclude that even though some of the assumptions behind the KJMA theory are not strictly fulfilled, it still provides a reasonable description of the phase-transformation kinetics of the Ising lattice gas. The effects of adsorbate diffusion can in part be accounted for by assuming a decaying nucleation rate. This effectively yields a crossover from continuous to instantaneous nucleation when diffusion is the predominant process.

4.4 Onset of the crossover

Our previous results have shown that a crossover of the nucleation from continuous to instantaneous sets in when the fit of the relaxation function to Eqs. (4), (6), and (15) results in a parameter $\lambda\tau$ of the order of one. Then, we find changes in the morphology of the adsorbate phase and a faster decrease of the microscopic nucleation rate. As commonly accepted in vacuum surface science, diffusion of adsorbed particles results in exclusion zones around existing clusters, in which nucleation is suppressed, since free particles rather aggregate to the cluster than form a new nucleus. Our hypothesis is that these exclusion zones become space-filling at early times for high diffusion rates [9]. Here we present a rough estimate of when the crossover sets in.

The average distance between independent droplets is roughly [23]

$$R_0 \approx v\tau. \tag{21}$$

From the competition between desorption and diffusion, a monomer after the time it adsorbs performs on average

$$N(\infty) = \frac{p_{\text{dif}}}{p_{\text{des}}} \tag{22}$$

steps. Here, from Eq. (10) $p_{\text{dif}} = \nu_0 \exp(-\Delta_{\text{dif}}/k_{\text{B}}T)$ is the diffusion probability of a free monomer, and $p_{\text{des}} = \nu \exp(-\Delta_{\text{ad/des}}/k_{\text{B}}T) \exp(-\mu/2 k_{\text{B}}T)$ with $\mu = (\mu - \mu_0) - 2\Phi$ is its desorption probability. In a two-dimensional random walk the particle travels a distance $\sqrt{N(\infty)}$. We compare $\sqrt{N(\infty)}$ and R_0 in Table 9. For $\Delta_{\text{dif}} = 15$ the monomer performs on average less than one step. The crossover to instantaneous nucleation is complete when the diffusion length of a monomer is about half the average cluster distance. Despite the crudeness of the approximation it gives a satisfactory explanation for the onset of the crossover. It correctly reproduces the trends with supersaturation and diffusion barrier.

5 Summary and Conclusions

We have performed kinetic Monte Carlo simulations of the adsorption dynamics of a monolayer in a square lattice-gas model using Arrhenius dynamics with local barriers. The model Hamiltonian is grand-canonical, meaning that local adsorption/desorption equilibrium is approximately established. This makes it suitable for submonolayer electrochemical deposition under control of the potential difference between solution and electrode and when mass-transport limitations to the surface are insignificant. The elementary steps included in

the model are adsorption, desorption, and diffusion; our main interest is in the influence of the latter on the phase-transformation dynamics. The diffusion rates can be controlled by the barrier height for the diffusion steps. We have obtained results for the phase-transformation kinetics, the adsorbate morphology, and the microscopic rates of nucleation, cluster growth (interface velocity), and coalescence. For our model calculations we have used an extension of Bortz et al.'s n -fold way algorithm that contains both adsorption (spin-flip) and diffusion (spin-exchange), and whose details we present in this paper.

The nucleation rate and the interface velocity and consequently the phase-transformation kinetics are accelerated by both an increase of the supersaturation (the driving force) and the diffusion rate. The higher the diffusion rate, the more likely it is that a walker aggregates with sub- or supercritical clusters to participate in nucleation or growth, respectively.

Around supercritical clusters, diffusion causes a local reduction of the nucleation rate in a zone with the extension of the monomer diffusion length, since it is more likely that monomers reach the existing cluster than that they create a new one. This causes a reduction of the cluster density and an increase of the correlation length. Moreover, diffusion changes the spatial correlation between the nuclei, which is no longer random, and creates minima in the two-point correlation functions.

For a theoretical description of the phase transformation we use the Kolmogorov-Johnson-Mehl-Avrami (KJMA) theory as a coarse-grained approximation to our microscopic model system. The theory is based on the assumption that nucleation is spatially random. Using an appropriate law for the time dependence of the nucleation rate, one can obtain an estimate for Iv^2 from a fit of the time dependence of the relaxation function of the metastable phase, but no separate estimates for the nucleation rate I and the interface velocity v . In the absence of diffusion, this gives very accurate results assuming a constant extended nucleation rate I (continuous nucleation), even though our microscopic results suggest that the real nucleation rate decreases somewhat too fast with time for this assumption to be strictly fulfilled. With diffusion, though, the exclusion zones around supercritical clusters grow with the cluster radius, such that the real nucleation rate diminishes more strongly with time than expected from the decrease of the free surface fraction (and than in the case without diffusion). Assuming an extended nucleation rate that decreases exponentially with time from an initial value I_0 , we can extend the analysis to this case and still extract an estimate for I_0v^2 . This estimate is less accurate, but still correct by order of magnitude. We emphasize that correlation effects, which are also important in these cases, are neglected, since we use Avrami's law. When diffusion is predominant, the exclusion zones become space-filling at early times of the phase transformation, and the dynamics resemble in-

stantaneous nucleation. A fit to the respective form of Avrami’s law would, however, not yield an estimate for I_0v^2 . Instead, I_0v^2/λ is obtained from this analysis, where λ is the time constant of the decay of I . I_0/λ is the density of nuclei. We emphasize that nucleation is still homogeneous. Hence, in the electrodeposition of a two-dimensional film that proceeds by a first-order phase transition, instantaneous nucleation need not imply heterogeneous nucleation at defects. Also, intermediate cases are possible that would lead to non-linear Avrami plots and non-integer Avrami exponents. A strong indication for our model to be a good description of a given experimental system could be found in the two-point correlation functions, which develop minima for an Avrami exponent less than 3. They can be obtained from scattering experiments [44] or by analysis of microscopic images.

In the absence of diffusion, it is possible to obtain separate estimates for I and v from the variance of the coverage *vs.* time using Sekimoto’s theory for the two-point correlation function. This theory is based on spatially random nucleation as well, and the analysis breaks down when diffusion rates become noticeable and a minimum in the correlation function appears.

The time a walker spends on the surface before it desorbs increases with higher supersaturation, such that in this case the influence of diffusion on the dynamics of the phase transformation at the same rate is stronger. Hence, the crossover to instantaneous nucleation is more complete for the same diffusion barrier when the supersaturation is greater.

In a previous work [9] we have presented kinetic Monte Carlo simulations of the same model using Glauber dynamics, but without varying the supersaturation, and performing a less stringent analysis of the data. Still, we found from the time-dependence of the relaxation function qualitatively the same crossover to instantaneous nucleation as in the present investigation. In various studies for solid-on-solid (SOS) and Ising models, a comparison of different transition probabilities in kinetic Monte Carlo dynamics has shown that the stochastic dynamics can have a strong influence on the microscopic properties of the evolving system, namely interfacial structure, nucleation rates, and interface velocities (see, e.g., Refs. [42, 45, 46]). Distinctions are made between so-called “soft” dynamics, in which the field (supersaturation) and coupling (interaction) constant terms in the transition probability factorize, and “hard” dynamics, in which they do not. The dynamics in the present work are soft, while in Ref. [9] they are hard. Another difference is that here we use local barriers in contrast to Ref. [9]. In both investigations, the stochastic dynamics contain conserving and non-conserving steps with respect to the order parameter (the coverage). This paper does not aim at a systematic investigation of the influence of the stochastic dynamics; in fact the diffusion is treated in such different ways that a quantitative comparison is difficult. It is, however, possible to conclude that the decrease in local nucleation rates around clus-

ters and the concomitant development of spatial correlations translate into qualitatively similar changes in the phase-transformation dynamics.

Acknowledgements

This work was supported by the U.S. National Science Foundation under Grant No. DMR-0240078, and by Florida State University through its Center for Materials Research and Technology and its School of Computational Science. S.F.'s work in Ulm is supported by the Deutsche Forschungsgemeinschaft under Grant No. HA 5159/1-1

Appendix

Here we introduce our single-site n -fold way scheme for the square lattice-gas model with both adsorption/desorption and diffusion steps. For computational convenience, we present the classification scheme in Ising language, $s = +1$ representing a spin up (occupied site) and $s = -1$ representing a spin down (empty site). For the sake of consistency, we also present the energy differences in terms of the Ising Hamiltonian. Within Ising terminology, adsorption/desorption is equivalent to spin flip and diffusion to spin exchange. The former involves only one particle, while the latter involves a pair. Hence, care must be taken that diffusion steps are not counted twice when we set up our list of all elementary steps in the lattice. For each particle, only spin exchange with two of the four nearest neighbors in orthogonal directions (here: right and below, respectively) is to be considered. The spin exchange with the nearest neighbors in the opposite directions (left and above, respectively) is included in the neighbors' respective set of moves. In lattice-gas terms, instead of the diffusion of a particle to the left or upwards, we consider the diffusion of a vacancy to the right or downwards, starting from the respective nearest-neighbor position. We use the following labels for the three elementary steps associated with each lattice point: $m = 1$ (adsorption/desorption), $m = 2$ (diffusion to [spin exchange with] the nearest-neighbor position to the right, and $m = 3$ (diffusion to [spin exchange with] the nearest-neighbor position below). We call the classes for the adsorption/desorption steps particle classes and for the diffusion steps pair classes. For the particle classes, we need to consider the value (spin) s_i of the central particle C and of its four nearest neighbors, s_k . For the pair classes, we need to consider the spins s_i and s_j of two neighboring particles, C and C', respectively. C and C' form the pair S. Moreover, we consider the spins s_k of *all* nearest neighbors of C, and the spins s_l of *all* the nearest neighbors of C'. The central particle C is the one to which

the respective pair class belongs. C' is called the exchange partner.

For the particle classes $c_{a/d}$, the scheme is shown in Table A-1 [32]. From it follows the simple relation

$$c_{a/d} = \frac{1}{2} \left(11 - 5s_i - \sum_k s_k \right). \quad (\text{A-1})$$

The difference of the configurational energy resulting from the respective adsorption/desorption step is obtained from

$$\mathcal{H}(b) - \mathcal{H}(a) = \Delta\mathcal{H} = 2Js_i \sum_k s_k + 2Hs_i. \quad (\text{A-2})$$

For the pair classes c_{dif} , only the cases where $s_j \neq s_i$ need to be considered; the scheme is shown in Table A-2. It follows the simple relation

$$c_{\text{dif}} = -\frac{13}{2}s_i + 2 \sum_k s_k + \frac{1}{2} \sum_l s_l + \frac{33}{2}. \quad (\text{A-3})$$

The difference of the configurational energy performing the respective diffusion step is obtained from

$$\mathcal{H}(b) - \mathcal{H}(a) = \Delta\mathcal{H} = J \left[(s_i - s_j) \left(\sum_k s_k - \sum_l s_l \right) + 4 \right]. \quad (\text{A-4})$$

Not only are the classes changed by moves in which the respective site is involved, but also by moves in the neighborhood. The classes of up to some of the 4th-nearest neighbors have to be updated after a move. See Fig. A-1 for an overview of the sites affected by a move, and Fig. A-2 for the designation of the neighboring positions. We denote the spin of an affected site with t_i when it is the central particle X, and with t_j when it is the exchange partner X' of X. X and X' form the pair T. The spins of *all* the nearest neighbors of X and X' are labeled t_k and t_l , respectively. Tables A-3, A-4 and A-5 summarize how the classes in the neighborhood are affected.

References

- [1] L. Blum, D. A. Huckaby, M. Legault, *Electrochim. Acta* 41 (1996) 2207.
- [2] A. N. Kolmogorov, *Bull. Acad. Sci. USSR, Phys. Ser.* 1 (1937) 335.
- [3] W. A. Johnson, R. F. Mehl, *Trans. Am. Inst. Min. Metall. Eng.* 135 (1939) 416.
- [4] M. Avrami, *J. Chem. Phys.* 7 (1939) 1103.
- [5] M. Avrami, *J. Chem. Phys.* 8 (1940) 212.
- [6] M. Avrami, *J. Chem. Phys.* 9 (1941) 177.
- [7] W. Schmickler, *Interfacial Electrochemistry*, Oxford University Press, New York, Oxford (1996).
- [8] M. H. Hölzle, U. Retter, D. M. Kolb, *J. Electroanal. Chem.* 371 (1994) 101.
- [9] S. Frank, D. E. Roberts, P. A. Rikvold, *J. Chem. Phys.* 122 (2005) 064705.
- [10] E. Pineda, T. Pradell, D. Crespo, *Philos. Mag. A* 82 (2002) 107.
- [11] M. Fanfoni, M. Tomellini, *Eur. Phys. J. B* 34 (2003) 331.
- [12] G. Brown, P. A. Rikvold, S. J. Mitchell, M. A. Novotny, in: *Interfacial Electrochemistry: Theory, Experiment, and Applications*, ed. by A. Wieckowski, Marcel Dekker, New York (1999), pp. 47–61.
- [13] P. A. Rikvold, G. Brown, S. J. Mitchell, in: *Encyclopedia of Surface and Colloid Science*, ed. by A. Hubbard, Marcel Dekker, New York (2002), pp. 4814–4824.
- [14] M. I. Rojas, *Surf. Sci.* 569 (2004) 76.
- [15] K. Binder, D. W. Heermann, *Monte Carlo Simulations in Statistical Physics. An Introduction*, Springer, Berlin, 3rd edn. (1997).
- [16] H. C. Kang, W. H. Weinberg, *J. Chem. Phys.* 90 (1989) 2824.
- [17] K. A. Fichthorn, W. H. Weinberg, *J. Chem. Phys.* 95 (1991) 1090.
- [18] I. Abou Hamad, P. A. Rikvold, G. Brown, *Surf. Sci.* 572 (2004) L335.
- [19] A. Aramata, in: *Modern Aspects of Electrochemistry*, No. 31, ed. by J. O'M. Bockris, R. E. White, and B. E. Conway, Plenum Press, New York, London (1997), pp. 181–249.
- [20] G. Brown, P. A. Rikvold, M. A. Novotny, A. Wieckowski, *J. Electrochem. Soc.* 146 (1999) 1035.
- [21] N. B. Luque, E. P. M. Leiva, *Electrochim. Acta* 50 (2005) 3161.
- [22] P. A. Rikvold, B. M. Gorman, in: *Annual Reviews of Computational Physics*, vol. 1, ed. by D. Stauffer, World Scientific, Singapore (1994), pp. 149–191.

- [23] R. A. Ramos, P. A. Rikvold, M. A. Novotny, *Phys. Rev. B* 59 (1999) 9053.
- [24] U. Evans, *Trans. Faraday Soc.* 41 (1945) 365.
- [25] M. Fanfoni, M. Tomellini, *Phys. Rev. B* 54 (1996) 9828.
- [26] V. Sessa, M. Fanfoni, M. Tomellini, *Phys. Rev. B* 54 (1996) 836.
- [27] M. Tomellini, M. Fanfoni, *Phys. Rev. B* 55 (1997) 14071.
- [28] V. Erukhimovitch, J. Baram, *Phys. Rev. B* 51 (1995) 6221.
- [29] L. Onsager, *Phys. Rev.* 65 (1944) 117.
- [30] T. Ala-Nissila, J. Kjoll, S. C. Ying, *Phys. Rev. B* 46 (1992) 846.
- [31] T. Ala-Nissila, S. C. Ying, *Prog. Surf. Sci.* 39 (1992) 227.
- [32] A. B. Bortz, M. H. Kalos, J. L. Lebowitz, *J. Comput. Phys.* 17 (1975) 10.
- [33] G. H. Gilmer, *J. Crystal Growth* 35 (1976) 1081.
- [34] J. Hoshen, R. Kopelman, *Phys. Rev. B* 14 (1976) 3438.
- [35] W. H. Press, S. A. Teukolsky, W. T. Vetterling, B. P. Flannery, *Numerical Recipes in Fortran 77*, Cambridge University Press, Cambridge, New York, 2nd edn. (1992).
- [36] J. D. Gunton, M. San Miguel, P. S. Sahni, in: *Phase Transitions and Critical Phenomena*, vol. 8, ed. by C. Domb and J. L. Lebowitz, Academic Press, New York (1983).
- [37] K. Sekimoto, *Physica A* 135 (1986) 328.
- [38] K. Sekimoto, *Int. J. Mod. Phys. C* 5 (1991) 1843.
- [39] P. Debye, H. R. Anderson, H. Brumberger, *J. Appl. Phys.* 28 (1957) 679.
- [40] G. Brown, P. A. Rikvold, M. Sutton, M. Grant, *Phys. Rev. E* 60 (1999) 5151.
- [41] D. P. Landau, K. Binder, *A Guide to Monte Carlo Simulations in Statistical Physics*, Cambridge University Press, Cambridge (2000).
- [42] G. M. Buendía, P. A. Rikvold, M. Kolesik, *Phys. Rev. B* 73 (2006) 045437.
- [43] V. N. Smelyanskiy, M. I. Dykman, H. Rabitz, B. E. Vugmeister, S. L. Bernasek, A. B. Bocarsly, *J. Chem. Phys.* 110 (1999) 11488.
- [44] S. J. Mitchell, G. Brown, P. A. Rikvold, *Surf. Sci.* 471 (2001) 125.
- [45] K. Park, P. A. Rikvold, G. M. Buendía, M. A. Novotny, *Phys. Rev. Lett.* 92 (2004) 015701.
- [46] G. M. Buendía, P. A. Rikvold, K. Park, M. A. Novotny, *J. Chem. Phys.* 121 (2004) 4193.

Figure captions

Fig. 1. Fraction of diffusion steps as a function of the coverage during adsorption of a monolayer. Diffusion barrier $\Delta_{\text{dif}} = 15$.

Fig. 2. Acceleration of the phase transformation with increasing electrochemical potential. $\Delta_{\text{dif}} = \infty$.

Fig. 3. Acceleration of the phase transformation with diffusion. $\mu - \mu_0 = 0.4$.

Fig. 4. Crossover from continuous to instantaneous nucleation for $\mu - \mu_0 = 1.2$. (a) Logarithmic plot of the relaxation function *vs.* the cube of the normalized time, as expected for continuous nucleation, Eqs. (2) and (4). (b) Same *vs.* the square of the normalized time, as expected for instantaneous nucleation, Eqs. (3) and (4). In both cases, the straight line is a guide to the eye.

Fig. 5. Fits of the relaxation function to Avrami's law for exponentially decaying nucleation rate. Dotted lines: simulations. Continuous lines: fits. The curves are, from right to left, for $\Delta_{\text{dif}} = \infty, 15, 10, 5$. $\mu - \mu_0 = 1.2$.

Fig. 6. Two-point correlation functions $G(r)$ as functions of the distance r for various coverages. (a) $\mu - \mu_0 = 0.4$, $\Delta_{\text{dif}} = \infty$. (b) $\mu - \mu_0 = 1.6$, $\Delta_{\text{dif}} = 5$. Note the different scale along the horizontal axis in the two parts.

Fig. 7. Correlation length l *vs.* θ , estimated from the inverse of the initial slope of the normalized correlation function $\tilde{G}(r)$. Thin lines: $\mu - \mu_0 = 0.4$. Bold lines: $\mu - \mu_0 = 1.6$.

Fig. 8. Cluster-size distribution for $\mu - \mu_0 = 1.6$ at coverage $\theta = 0.3$. The vertical line marks the critical cluster size n^* .

Fig. 9. Snapshots of the adsorbate phase during the phase transformation. From left to right: $\mu - \mu_0 = 0.4$, $\Delta_{\text{dif}} = \infty$; $\mu - \mu_0 = 0.4$, $\Delta_{\text{dif}} = 5$; $\mu - \mu_0 = 1.6$, $\Delta_{\text{dif}} = \infty$; $\mu - \mu_0 = 1.6$, $\Delta_{\text{dif}} = 5$. Upper row: $\theta = 0.3$. Lower row: $\theta = 0.7$.

Fig. 10. Nucleation and dissolution rates and net nucleation rate for a cutoff size equal to the critical cluster size (thin lines) and one diffusion length in n -space larger (bold lines). $\mu - \mu_0 = 0.4$, $\Delta_{\text{dif}} = 15$.

Fig. 11. Net nucleation and coalescence rates and net cluster formation rate. (a) $\Delta_{\text{dif}} = \infty$. (b) $\Delta_{\text{dif}} = 5$. In both cases, $\mu - \mu_0 = 1.2$. Note the different scales in the two parts.

Fig. 12. Net nucleation rate for various diffusion barriers. $\mu - \mu_0 = 1.2$.

Fig. 13. Net coalescence rate for various diffusion barriers. $\mu - \mu_0 = 1.2$.

Fig. 14. Probability distribution of the time between two nucleation events in the simulations of the metastable phase. $\mu - \mu_0 = 1.2$.

Fig. 15. The kinetic parameter Iv^2 from the microscopic rates I and v and from the fit of the relaxation function to the theory.

Fig. A-1. (Color online) An overview of the affected classes of sites by a move of the central particle. (a) particle classes affected by adsorption/desorption: central site (red) and nearest neighbors (green). (b) particle classes affected by diffusion: the switching pair (red) and its nearest neighbors (green). (c) pair classes affected by adsorption/desorption: the pairs that contain the central particle (red) and those that contain one of its nearest neighbors (blue). (d) pair classes affected by diffusion: the diffusing pair (yellow), pairs that contain the central particle (red), pairs that contain the exchange partner (brown), pairs that contain nearest neighbors of the central particle (blue), of the exchange partner (pink), and of both (green). Bold arrows: the pair starts at the respective particle or nearest-neighbor site; thin arrows: the pair points to the respective site.

Fig. A-2. Designation of the affected nearest (NN), next-nearest (NNN), 3rd-nearest (3NN), and 4th-nearest (4NN) neighbor position when the central site undergoes a move. The numbers are the labels used in Tables A-3, A-4, and A-5.

Tables

Table 1

The average fraction of diffusion steps throughout the phase transformation.

$\mu - \mu_0$	$\Delta_{\text{dif}} = 15$	$\Delta_{\text{dif}} = 10$	$\Delta_{\text{dif}} = 5$
0.4	0.221	0.817	0.986
0.8	0.239	0.830	0.987
1.2	0.247	0.834	0.987
1.6	0.250	0.834	0.986

Table 2

The critical cluster size n^* as a function of the electrochemical potential.

$\mu - \mu_0$	n^*
0.4	18
0.8	7
1.2	4
1.6	3

Table 3

The metastable lifetime τ in MCSS. τ is the time when the relaxation function $\phi = 1/2$.

$\mu - \mu_0$	$\Delta_{\text{dif}} = \infty$	$\Delta_{\text{dif}} = 15$	$\Delta_{\text{dif}} = 10$	$\Delta_{\text{dif}} = 5$
0.4	270000	260000	216000	137000
0.8	59000	56800	49200	38800
1.2	27500	26800	24100	21300
1.6	16500	16200	15150	14300

Table 4

The kinetic parameter $I_0 v^2$ in MCSS⁻³, from a fit of the relaxation function ϕ to Avrami's law with an exponentially decaying nucleation rate.

$\mu - \mu_0$	$\Delta_{\text{dif}} = \infty$	$\Delta_{\text{dif}} = 15$	$\Delta_{\text{dif}} = 10$	$\Delta_{\text{dif}} = 5$
0.4	3.0×10^{-17}	3.3×10^{-17}	5.9×10^{-17}	3.3×10^{-16}
0.8	2.7×10^{-15}	3.0×10^{-15}	5.0×10^{-15}	1.9×10^{-14}
1.2	2.6×10^{-14}	2.8×10^{-14}	4.5×10^{-14}	1.2×10^{-13}
1.6	1.2×10^{-13}	1.2×10^{-13}	1.8×10^{-13}	4.0×10^{-13}

Table 5

The parameter $\lambda\tau$, from a fit of the relaxation function ϕ to Avrami's law with an exponentially decaying nucleation rate. $\lambda\tau$ indicates how much the extended nucleation rate I has decayed at the metastable lifetime. Standard errors are given in brackets below the values.

$\mu - \mu_0$	$\Delta_{\text{dif}} = \infty$	$\Delta_{\text{dif}} = 15$	$\Delta_{\text{dif}} = 10$	$\Delta_{\text{dif}} = 5$
0.4	6.7×10^{-3} (6.6×10^{-3})	1.1×10^{-4} (1×10^{-5})	2×10^{-2} (1×10^{-2})	1.70 (0.04)
0.8	8.3×10^{-5} (6×10^{-6})	7×10^{-5} (1×10^{-5})	0.36 (0.02)	3.52 (0.03)
1.2	5.8×10^{-5} (8×10^{-6})	3×10^{-2} (2×10^{-2})	0.65 (0.01)	4.13 (0.02)
1.6	6.9×10^{-5} (8×10^{-6})	1.5×10^{-4} (3×10^{-5})	0.79 (0.01)	4.20 (0.01)

Table 6

Nucleation rate per site and MCSS. Extended nucleation rate I from fit of $L^2 \text{var}(\theta)$ to Sekimoto's theory; real nucleation rate I_r from the maximum of the time-dependent net nucleation rate obtained from cluster counting; I_r from the initial slope of the density of supercritical clusters; and I_r from simulations of the metastable phase. For the simulations of the metastable phase, also the mean and standard deviation of the time in MCSS between nucleation events for the lattice size are given. For details of the methods, see the text.

$\mu - \mu_0$	Δ_{dif}	Sekimoto	microscopic	cluster density	metastable		
		I	I_r	I_r	I_r	$\langle t_{\text{nucl}} \rangle$	σ
0.4	∞	7.2×10^{-9}	1.4×10^{-8}	1.2×10^{-8}	2.8×10^{-8}	556.9	558.3
	15	8.3×10^{-9}	1.3×10^{-8}	1.1×10^{-8}	2.9×10^{-8}	528.3	523.4
	10	1.1×10^{-8}	1.8×10^{-8}	1.4×10^{-8}	3.8×10^{-8}	402.1	400.6
	5		3.0×10^{-8}	2.5×10^{-8}	8.7×10^{-8}	176.1	174.8
0.8	∞	1.6×10^{-7}	2.3×10^{-7}	2.1×10^{-7}	4.6×10^{-7}	33.2	33.2
	15	2.0×10^{-7}	2.5×10^{-7}	2.3×10^{-7}	4.9×10^{-7}	31.2	31.3
	10		3.1×10^{-7}	2.7×10^{-7}	6.6×10^{-7}	23.1	23.3
	5		4.3×10^{-7}	3.9×10^{-7}	1.2×10^{-6}	12.8	12.6

continued on next page

Table 6
continued

$\mu - \mu_0$	Δ_{dif}	Sekimoto	microscopic	cluster density	metastable		
		I	I_r	I_r	I_r	$\langle t_{\text{nucl}} \rangle$	σ
1.2	∞	6.4×10^{-7}	9.7×10^{-7}	9.1×10^{-7}	1.8×10^{-6}	8.5	8.5
	15	8.3×10^{-7}	1.1×10^{-6}	9.5×10^{-7}	1.9×10^{-6}	8.0	7.9
	10		1.2×10^{-6}	1.1×10^{-6}	2.5×10^{-6}	6.1	6.1
	5		1.5×10^{-6}	1.3×10^{-6}	3.9×10^{-6}	4.0	3.9
1.6	∞	1.8×10^{-6}	2.3×10^{-6}	2.1×10^{-6}	3.9×10^{-6}	4.0	3.9
	15	1.8×10^{-6}	2.4×10^{-6}	2.2×10^{-6}	4.1×10^{-6}	3.7	3.7
	10		2.7×10^{-6}	2.4×10^{-6}	5.1×10^{-6}	3.0	3.0
	5		2.9×10^{-6}	2.6×10^{-6}	7.0×10^{-6}	2.2	2.2

Table 7

Interface velocity v in unit length per MCSS. From fit of $L^2 \text{var}(\theta)$ to Sekimoto's theory; from the increase of the effective radius of the clusters during the initial phase of the simulation (standard deviation in parentheses); solid-on-solid interface from a dynamic mean-field approximation [42]. For details of the methods, see the text.

$\mu - \mu_0$	Δ_{dif}	Sekimoto	microscopic	(standard deviation)	MFA
0.4	∞	6.5×10^{-5}	5.3×10^{-5}	(2.8×10^{-5})	4.26×10^{-5}
	15	6.4×10^{-5}	5.5×10^{-5}	(2.8×10^{-5})	
	10	7.4×10^{-5}	7.0×10^{-5}	(3.3×10^{-5})	
	5		1.4×10^{-4}	(5.5×10^{-5})	
0.8	∞	1.3×10^{-4}	1.3×10^{-4}	(8.0×10^{-5})	8.58×10^{-5}
	15	1.2×10^{-4}	1.3×10^{-4}	(8.1×10^{-5})	
	10		1.8×10^{-4}	(9.9×10^{-5})	
	5		4.0×10^{-4}	(1.6×10^{-4})	
1.2	∞	2.0×10^{-4}	1.8×10^{-4}	(1.3×10^{-4})	1.30×10^{-4}
	15	1.8×10^{-4}	2.0×10^{-4}	(1.4×10^{-4})	
	10		2.9×10^{-4}	(1.7×10^{-4})	
	5		6.7×10^{-4}	(2.8×10^{-4})	

continued on next page

Table 7
continued

$\mu - \mu_0$	Δ_{dif}	Sekimoto	microscopic	(standard deviation)	MFA
1.6	∞	2.5×10^{-4}	2.3×10^{-4}	(1.9×10^{-4})	1.76×10^{-4}
	15	2.6×10^{-4}	2.5×10^{-4}	(1.9×10^{-4})	
	10		3.9×10^{-4}	(2.4×10^{-4})	
	5		9.4×10^{-4}	(3.8×10^{-4})	

Table 8

Ratio of nucleation rate I_0 and fitting parameter λ as estimate for the density of nuclei, which is approximated by the maximum density of supercritical clusters. $\Delta_{\text{dif}} = 5$.

$\mu - \mu_0$	I_0/λ	$\max(\rho_{\text{supercrit}})$
0.8	4.7×10^{-3}	3.1×10^{-3}
1.2	7.5×10^{-3}	5.4×10^{-3}
1.6	9.7×10^{-3}	7.1×10^{-3}

Table 9

Estimate of the onset of the crossover in the phase-transformation dynamics. Diffusion steps of a monomer before desorption $N(\infty)$; diffusion length of a monomer $l_d = \sqrt{N(\infty)}$; average distance between clusters R_0 .

$\mu - \mu_0$	Δ_{dif}	$N(\infty)$	l_d	R_0	l_d/R_0
0.4	15			14.3	
	10	1.9	1.4	15.1	0.09
	5	30.4	5.5	19.2	0.29
0.8	15			7.4	
	10	2.2	1.5	8.9	0.17
	5	34.0	5.8	15.5	0.37
1.2	15			5.4	
	10	2.4	1.6	7.0	0.23
	5	38.0	6.2	14.3	0.43
1.6	15			4.1	
	10	2.7	1.6	5.9	0.27
	5	42.4	6.5	13.4	0.49

Table A-1

The particle classes for the adsorption/desorption step

s_i	$\sum_k s_k$	$c_{a/d}$	$\Delta\mathcal{H}$
1	4	1	$2H + 8J$
	2	2	$2H + 4J$
	0	3	$2H$
	-2	4	$2H - 4J$
	-4	5	$2H - 8J$
-1	4	6	$-2H - 8J$
	2	7	$-2H - 4J$
	0	8	$-2H$
	-2	9	$-2H + 4J$
	-4	10	$-2H + 8J$

Table A-2

The pair classes for the diffusion step

s_i	s_j	$\sum_k s_k$	$\sum_l s_l$	c_{dif}	$\Delta\mathcal{H}$
1	-1	-4	-2	1	0
			0	2	$-4J$
			2	3	$-8J$
			4	4	$-12J$
		-2	-2	5	$4J$
			0	6	0
			2	7	$-4J$
			4	8	$-8J$
		0	-2	9	$8J$
			0	10	$4J$
			2	11	0
			4	12	$-4J$
		2	-2	13	$12J$
			0	14	$8J$
			2	15	$4J$
			4	16	0

continued on next page

Table A-2
continued

s_i	s_j	$\sum_k s_k$	$\sum_l s_l$	c_{dif}	$\Delta\mathcal{H}$
-1	1	-2	-4	17	0
			-2	18	$4J$
			0	19	$8J$
			2	20	$12J$
		0	-4	21	$-4J$
			-2	22	0
			0	23	$4J$
			2	24	$8J$
		2	-4	25	$-8J$
			-2	26	$-4J$
			0	27	0
			2	28	$4J$
		4	-4	29	$-12J$
			-2	30	$-8J$
			0	31	$-4J$
			2	32	0

Table A-3

Update of the particle classes $c_{a/d}$ after a move: $c_{\text{new}} = c_{\text{old}} + \Delta c$. For the designation of the spins and particles, see the text. For the meaning of the symbols for the site, see Fig. A-2.

move	description	Δc	site
a/d	X is C	$+5s_{i,\text{old}}$	central
	X is NN of C	$+s_{i,\text{old}}$	NN 0, 1, 2, 3
dif	X is C	$+4s_{i,\text{old}}$	central* \dagger
	X is C'	$+4s_{j,\text{old}}$	NN 1*
			NN 3 \dagger
	NN of X is C	$+s_{i,\text{old}}$	NN 0, 2, 3*
			NN 0, 1, 2 \dagger
	NN of X is C'	$+s_{j,\text{old}}$	NNN 1, 2; 3NN 1*
NNN 1, 3; 3NN 3 \dagger			

* move was diffusion to the right: C' is NN 1

\dagger move was diffusion to site below: C' is NN 3

Table A-4

Update of the pair classes after an adsorption/desorption move: $c_{\text{new}} = c_{\text{old}} + \Delta c$. $m = 2$: affected class is c_{dif} for diffusion to nearest-neighbor position to the right (NN 1); $m = 3$: affected class is c_{dif} for diffusion to nearest-neighbor position below (NN 3). For the designation of the spins and particles, see the text. For the meaning of the symbols for the site, see Fig. A-2.

description	Δc	site	
		$m = 2$	$m = 3$
X is C	$-32s_{i,\text{old}}t_j$	central	central
X' is C	$-32s_{i,\text{old}}t_i - 16s_{i,\text{old}}$	NN 0	NN 2
NN of X is C	$-4s_{i,\text{old}}$	NN 1, 2, 3	NN 0, 1, 3
NN of X' is C	$-s_{i,\text{old}}$	NNN 0, 3; 3NN 0	NNN 0, 2; 3NN 2

Table A-5

Update of the pair classes after a diffusion move: $c_{\text{new}} = c_{\text{old}} + \Delta c$. $m = 2$: affected class is c_{dif} for diffusion to nearest-neighbor position to the right (NN 1); $m = 3$: affected class is c_{dif} for diffusion to nearest-neighbor position below (NN 3). For the designation of the spins, particles and pairs, see the text. For the meaning of the symbols for the site, see Fig. A-2.

description	Δc	site	
		$m = 2$	$m = 3$
T is S	$+16s_{i,\text{old}}$	central *	central \dagger
X is C, T \perp S	$-32s_{i,\text{old}}t_j + 4s_{i,\text{old}}$	central \dagger	central *
X' is C	$-32s_{i,\text{old}}t_i - 15s_{i,\text{old}}$	NN 0 * \dagger	NN 2 * \dagger
X is C'	$-32s_{j,\text{old}}t_j + 4s_j$	NN 1 *	NN 1 *
		NN 3 \dagger	NN 3 \dagger
X' is C'	$-32s_{j,\text{old}}t_i - 15s_{j,\text{old}}$	NNN 3 \dagger	NNN 2 *
T \parallel S	$-3s_{i,\text{old}}$	NN 2, 3 *	NN 0, 1 \dagger
NN of X is C	$-4s_{i,\text{old}}$	NN 1, 2 \dagger	NN 0, 3 *
NN of X' is C	$-s_{i,\text{old}}$	NNN 0, 3; 3NN 0 *	NNN 1; 3NN 1 *
		NNN 0; 3NN 0 \dagger	NNN 1, 3; 3NN 3 \dagger
NN of X is C'	$-s_{i,\text{old}}$	NNN 1, 2; 3NN 1 *	NNN 0; 3NN 2 *
		NNN 1; 3NN 3 \dagger	NNN 0, 2; 3NN 2 \dagger
NN of X' is C'	$-s_{i,\text{old}}$	4NN 0, 3 \dagger	4NN 1, 2 *

* move was diffusion to the right: C' is NN 1

\dagger move was diffusion to site below: C' is NN 3

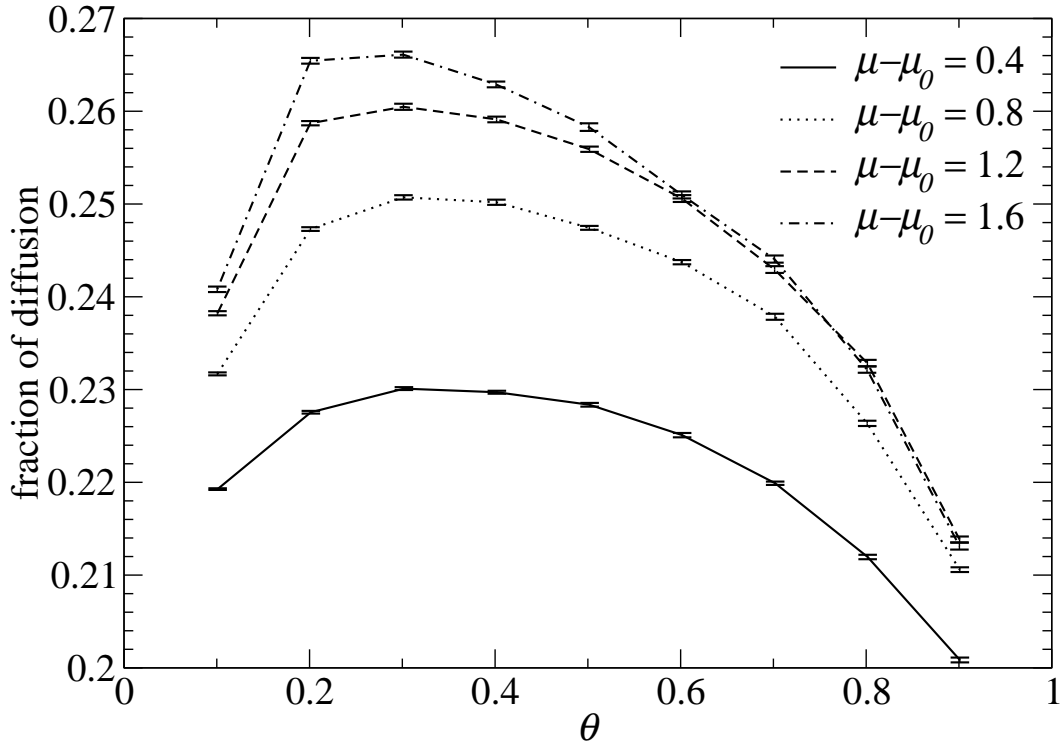


Fig. 1.

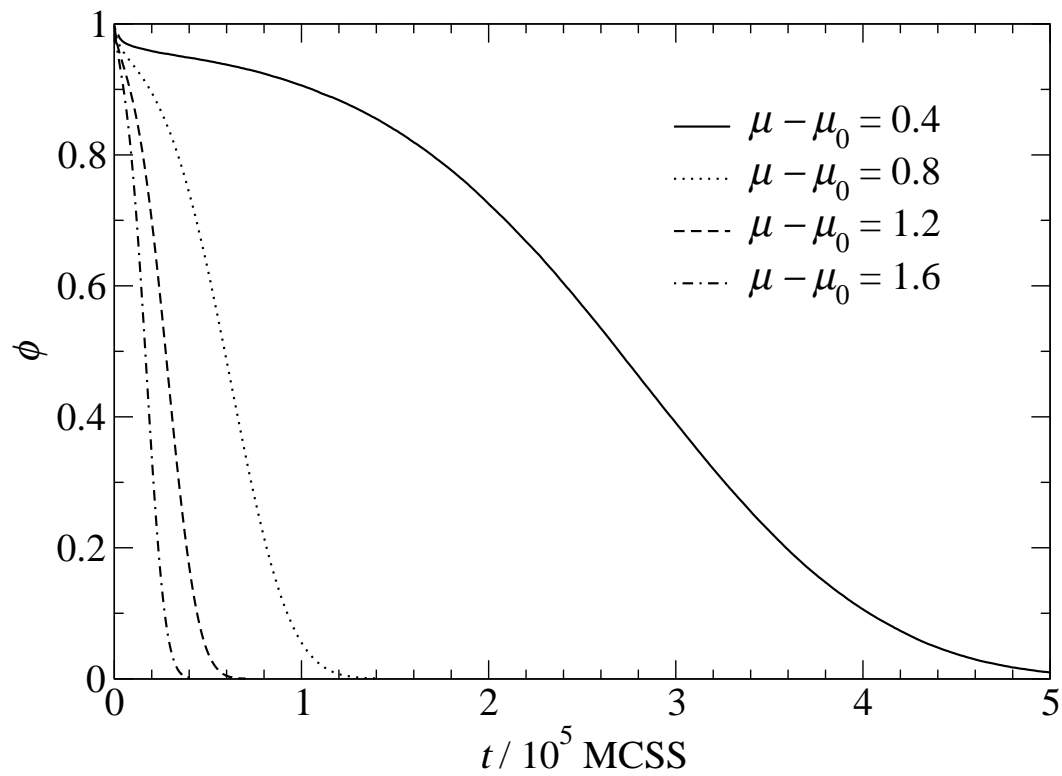


Fig. 2.

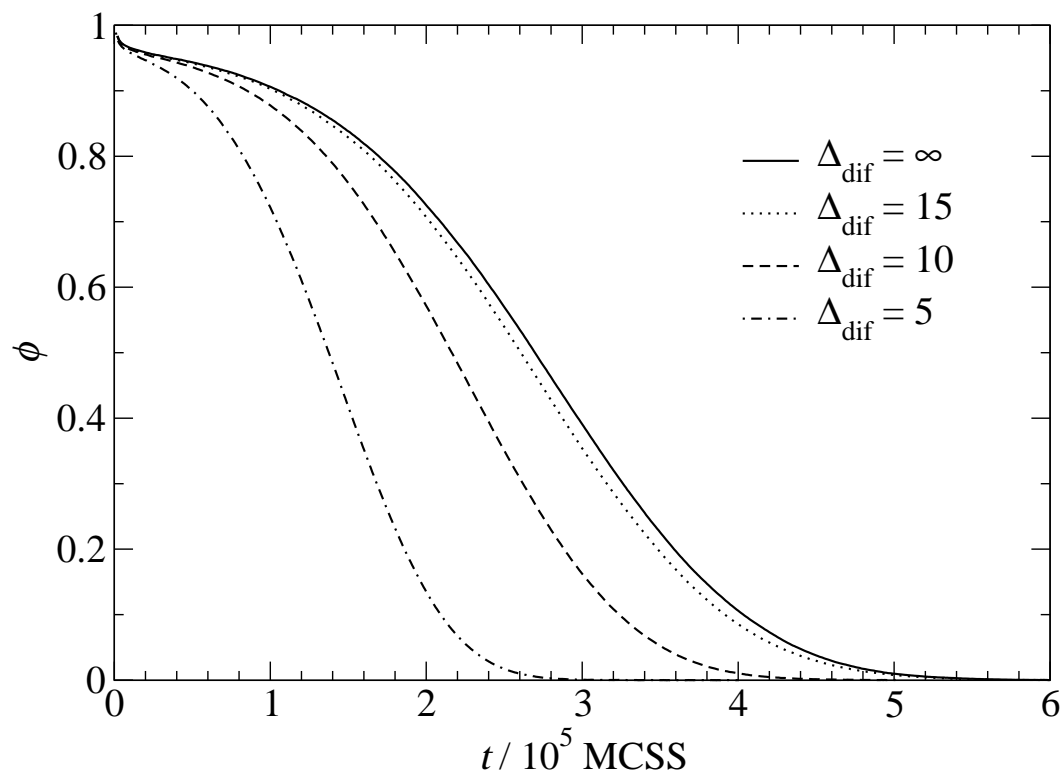


Fig. 3.

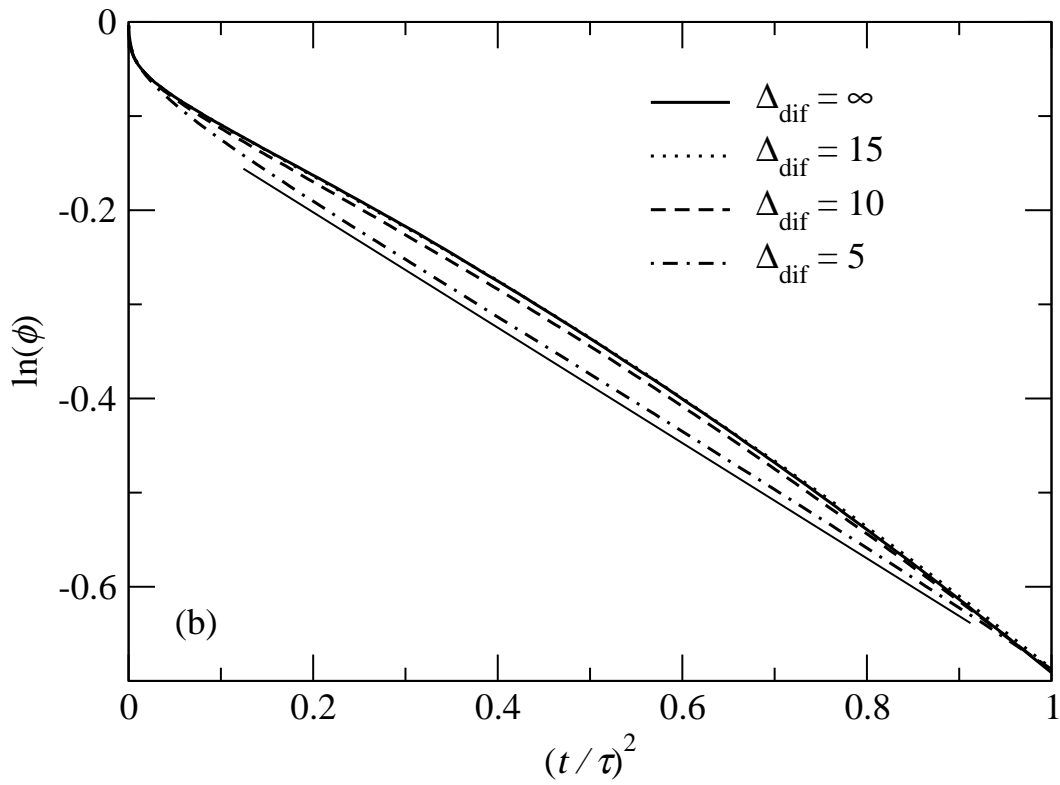
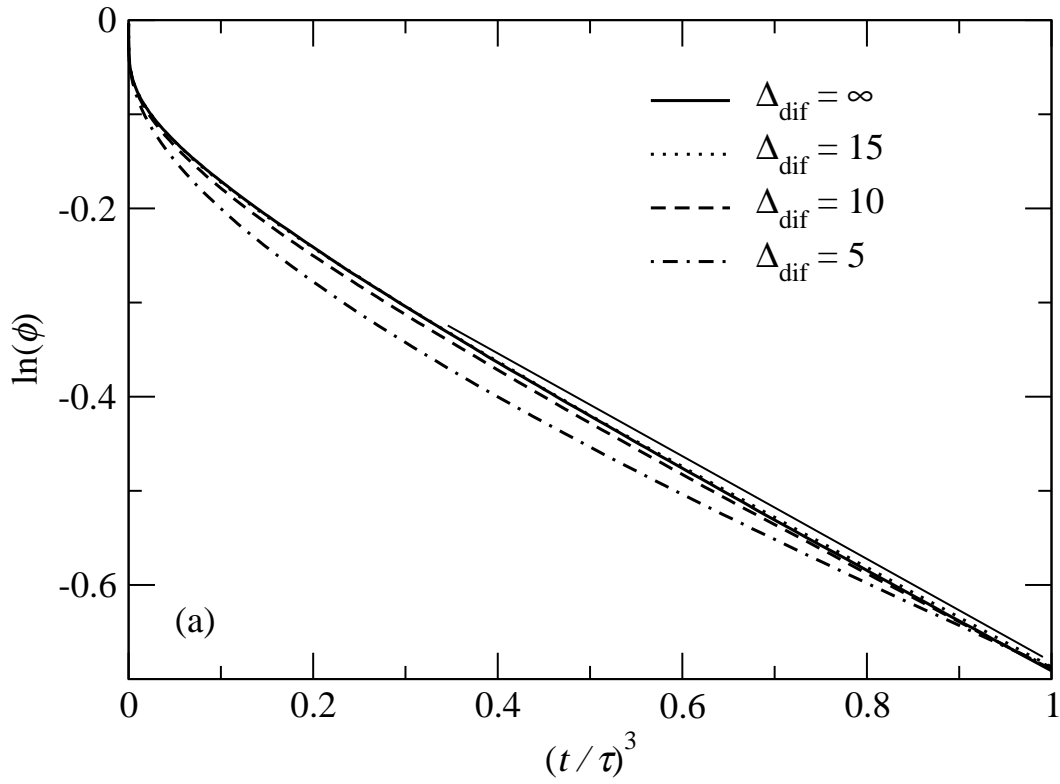


Fig. 4.

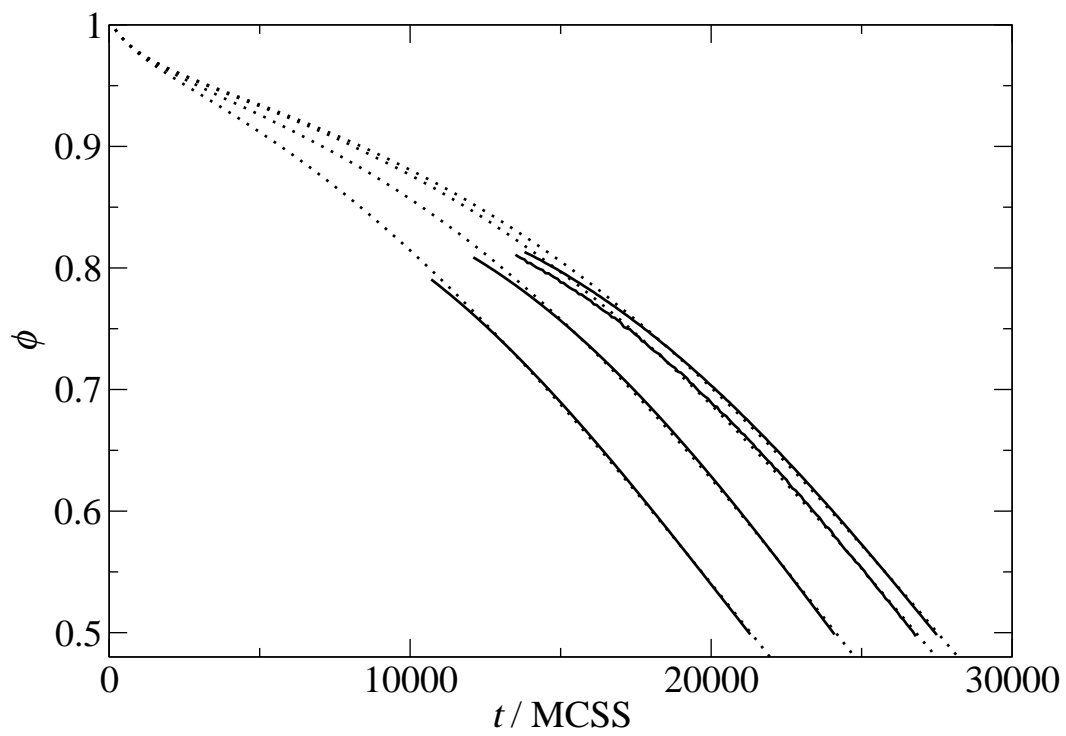


Fig. 5.

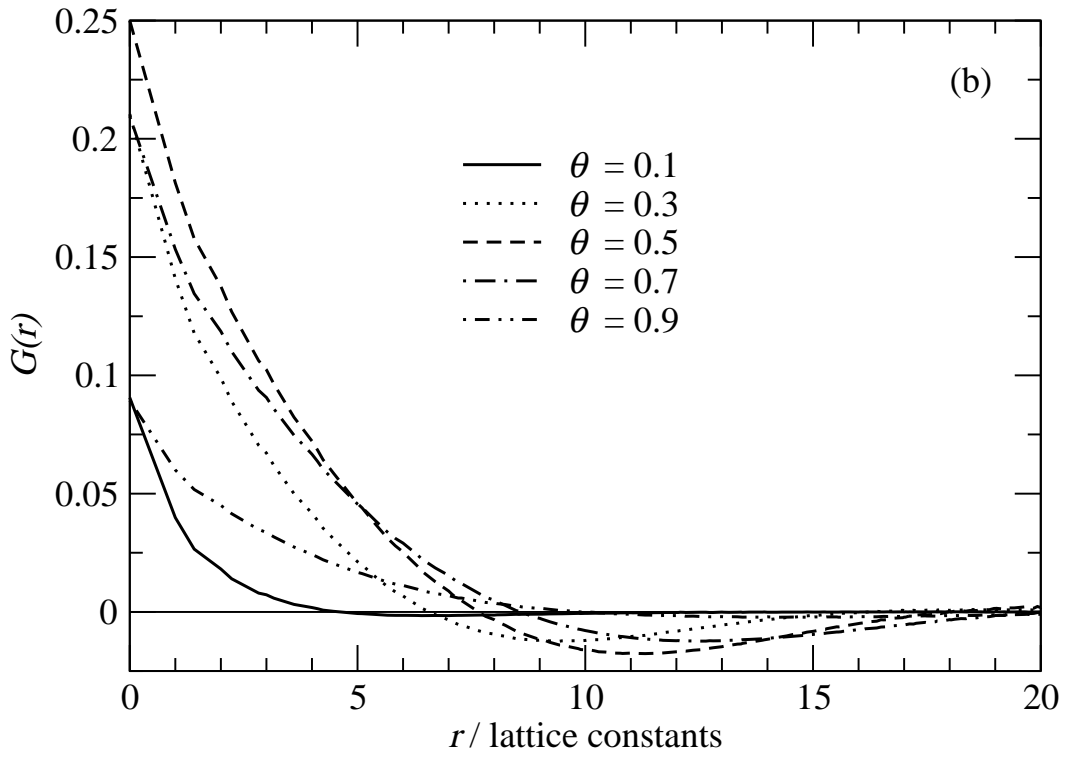
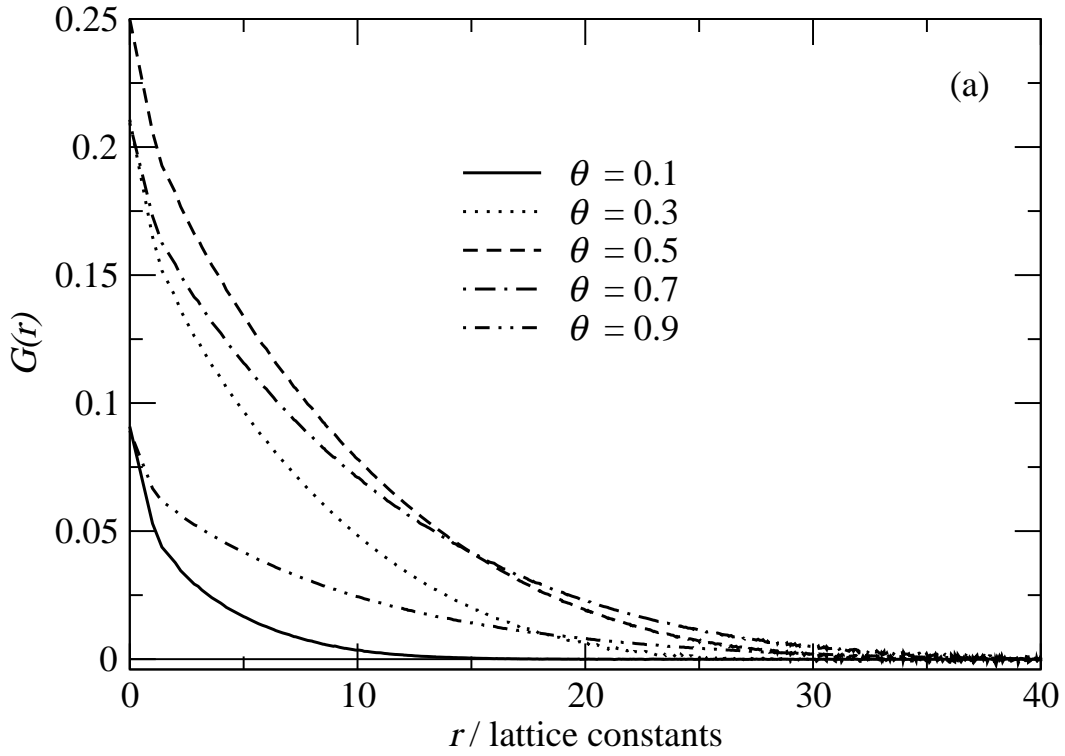


Fig. 6.

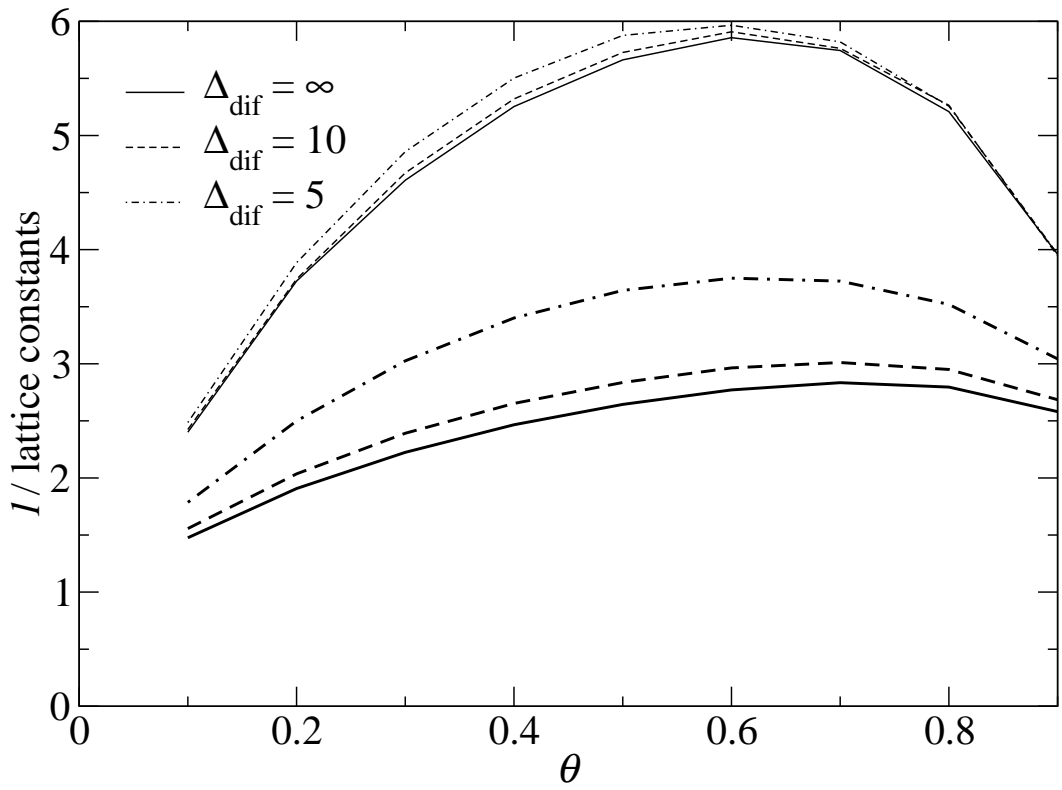


Fig. 7.

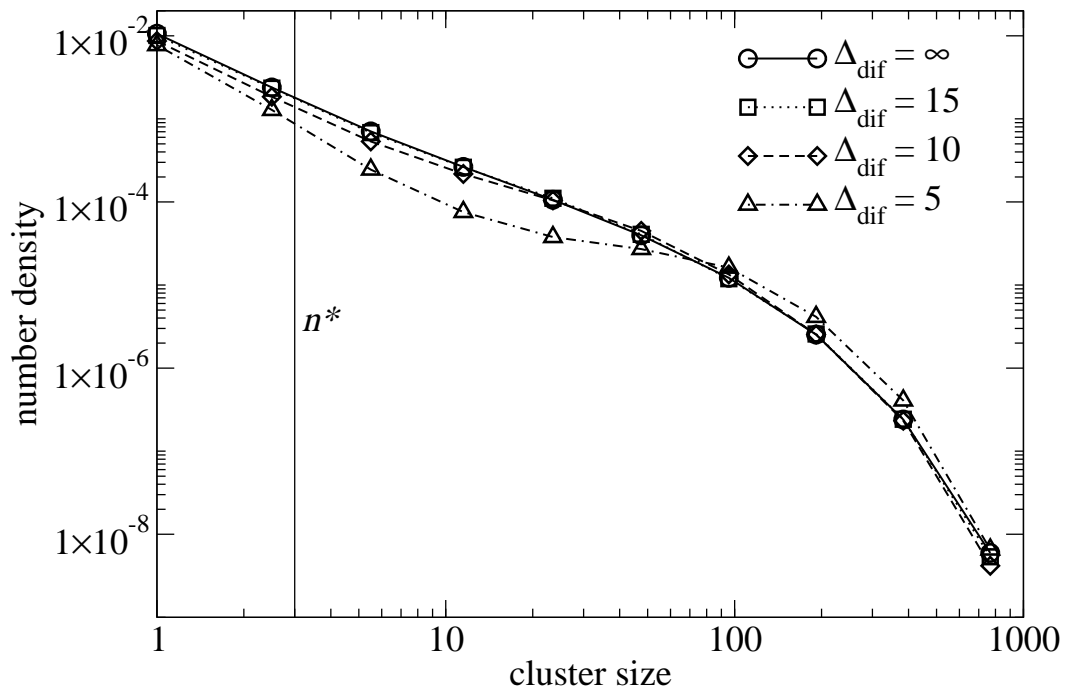


Fig. 8.

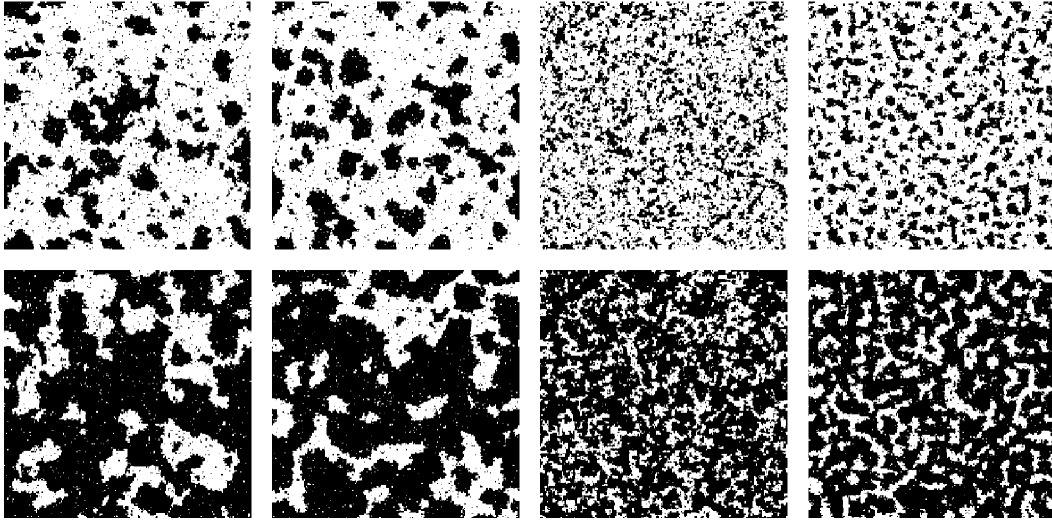


Fig. 9.

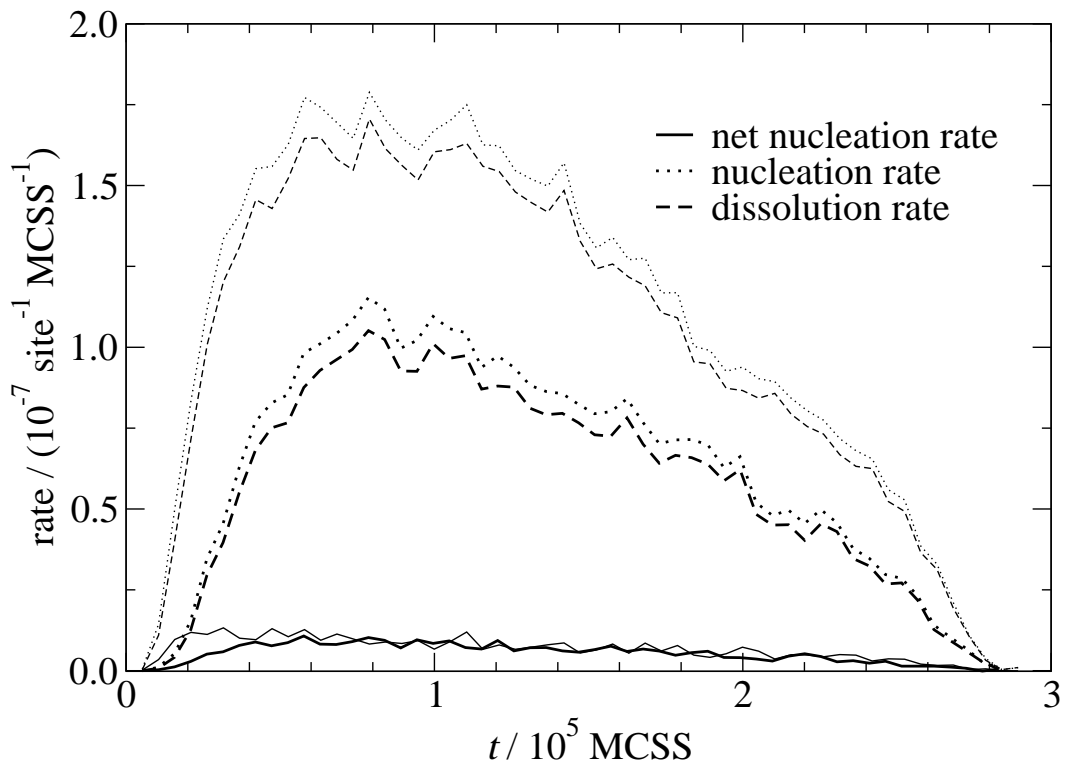


Fig. 10.

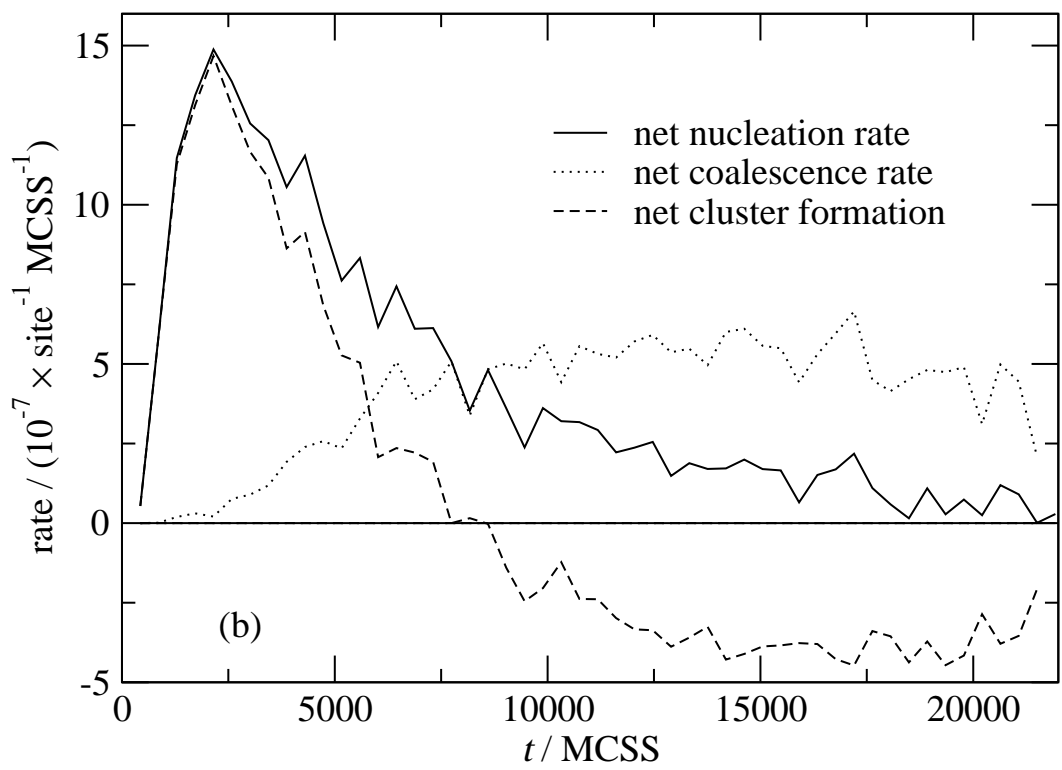
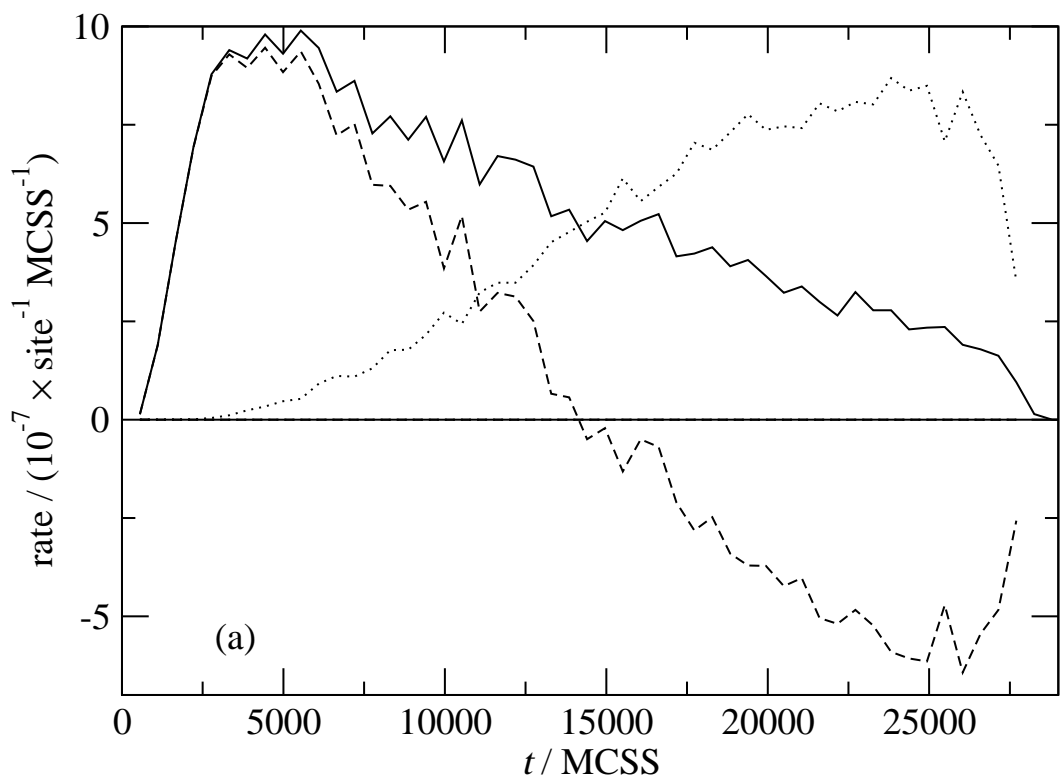


Fig. 11.

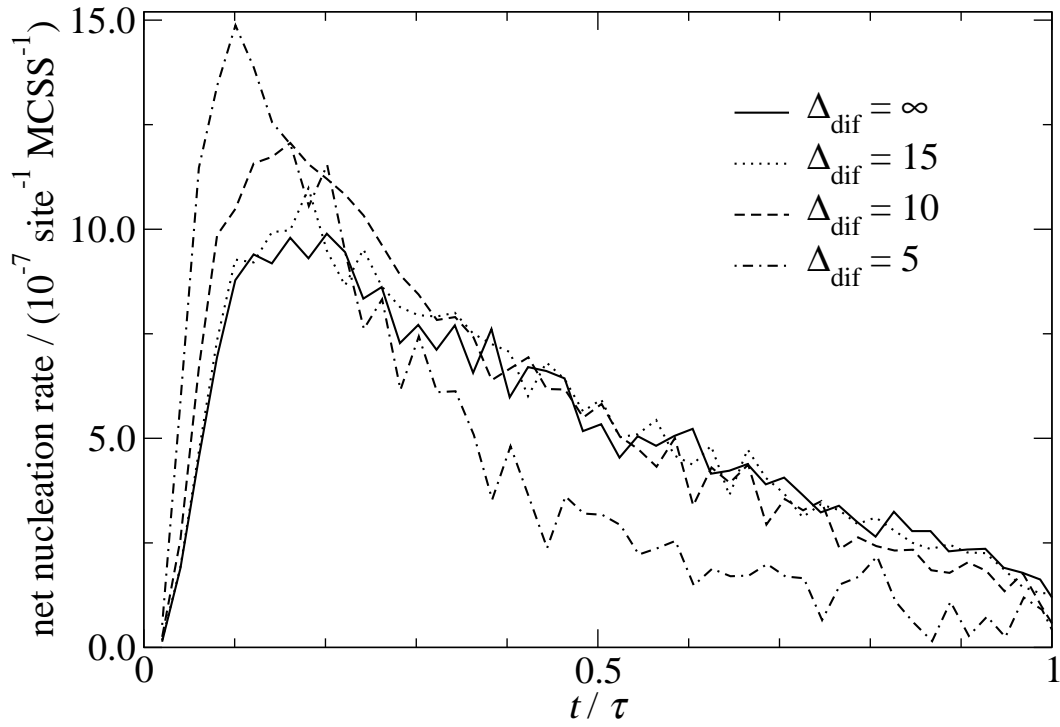


Fig. 12.

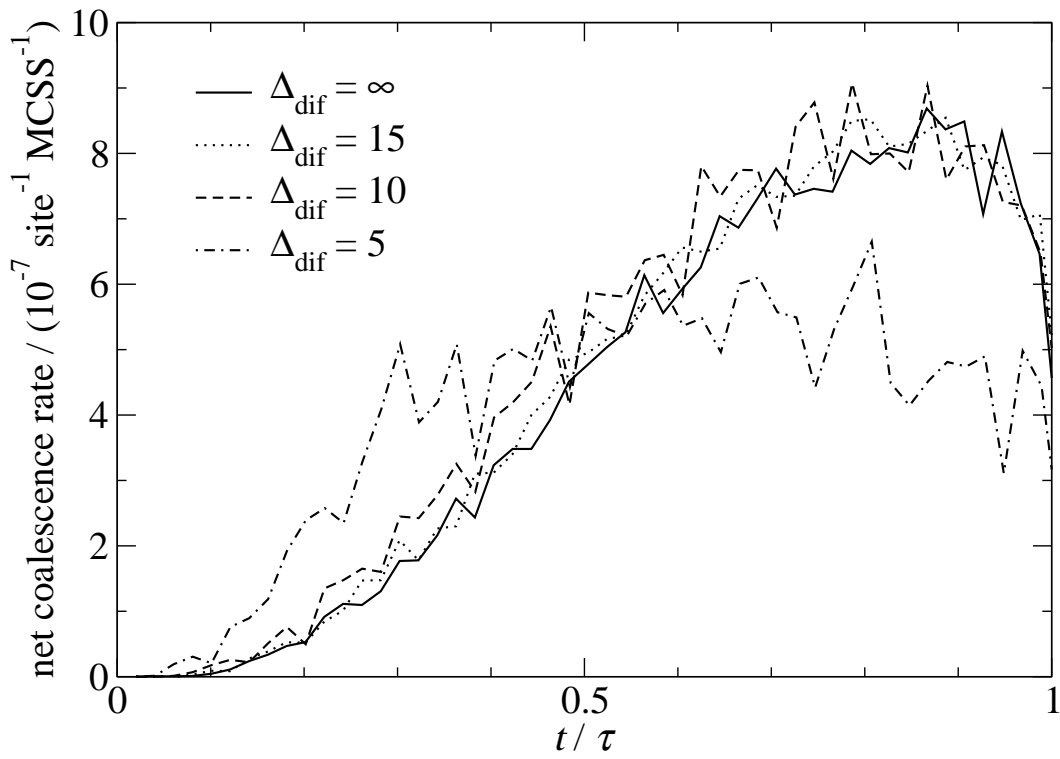


Fig. 13.

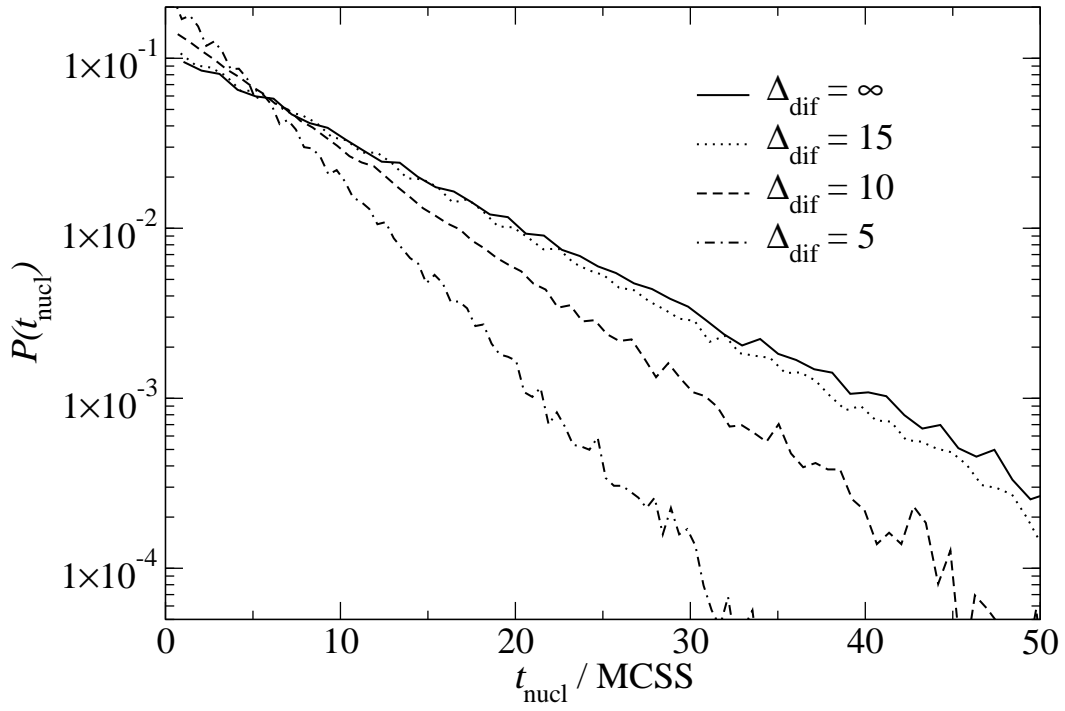


Fig. 14.

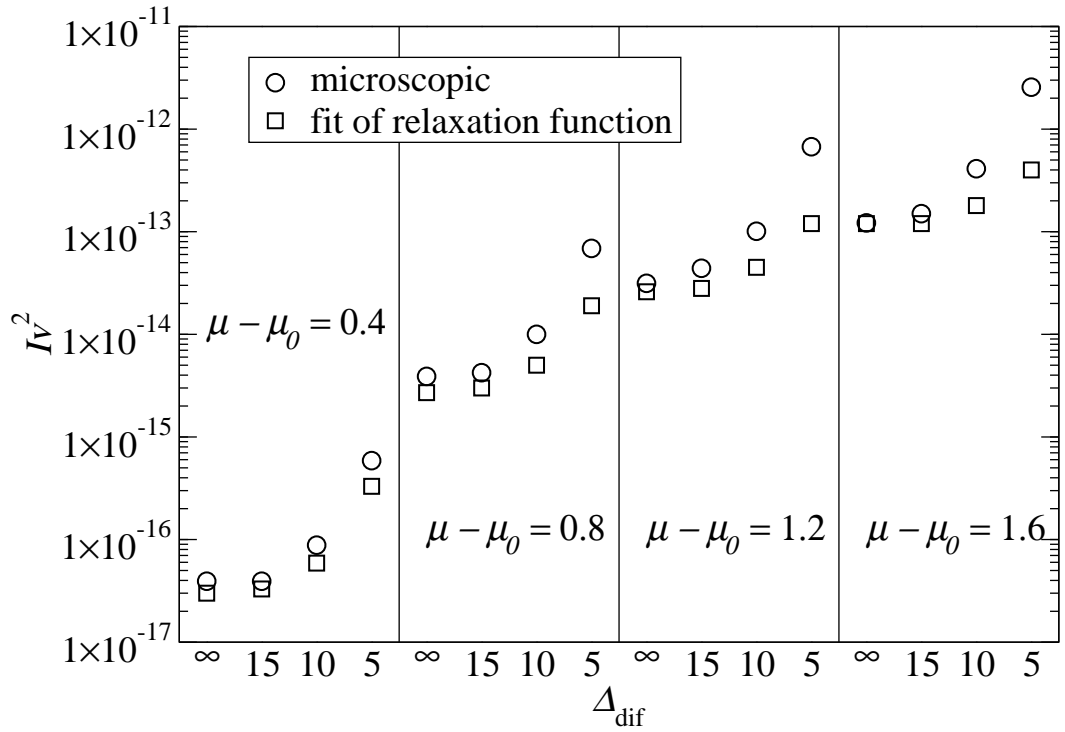


Fig. 15.

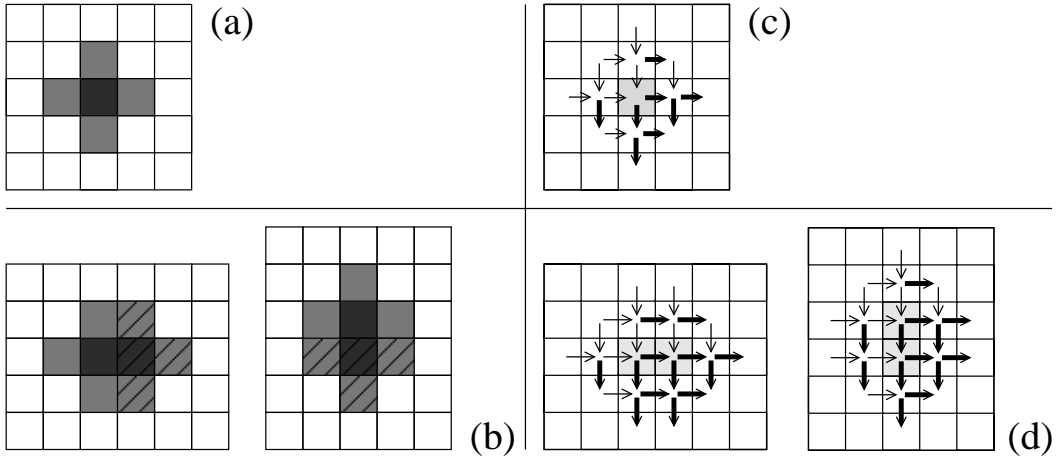


Fig. A-1. (greyscale)

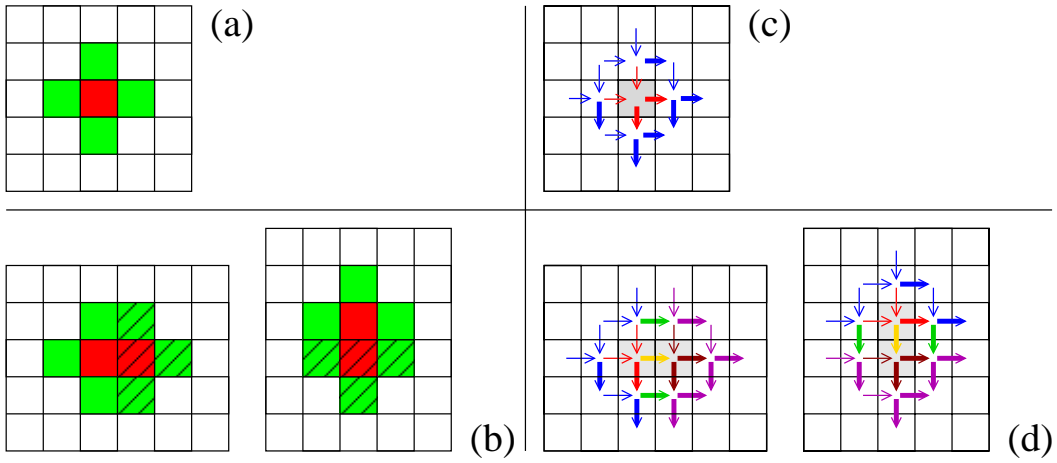


Fig. A-1. (color)

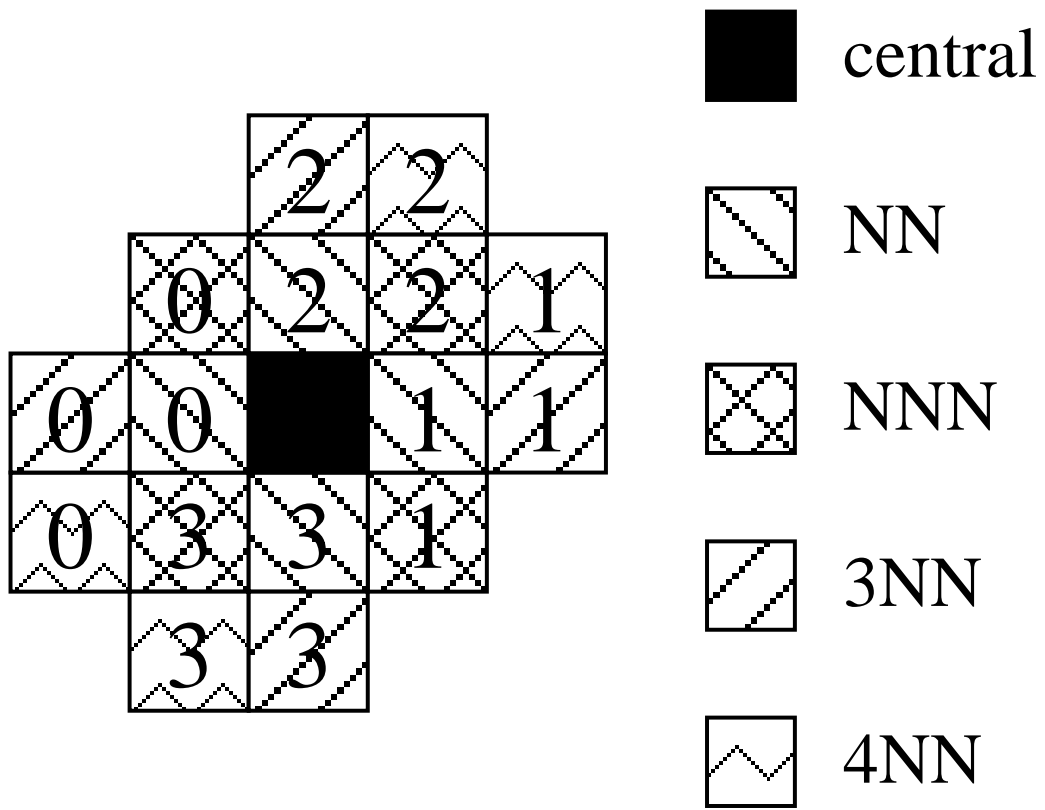


Fig. A-2. (greyscale)

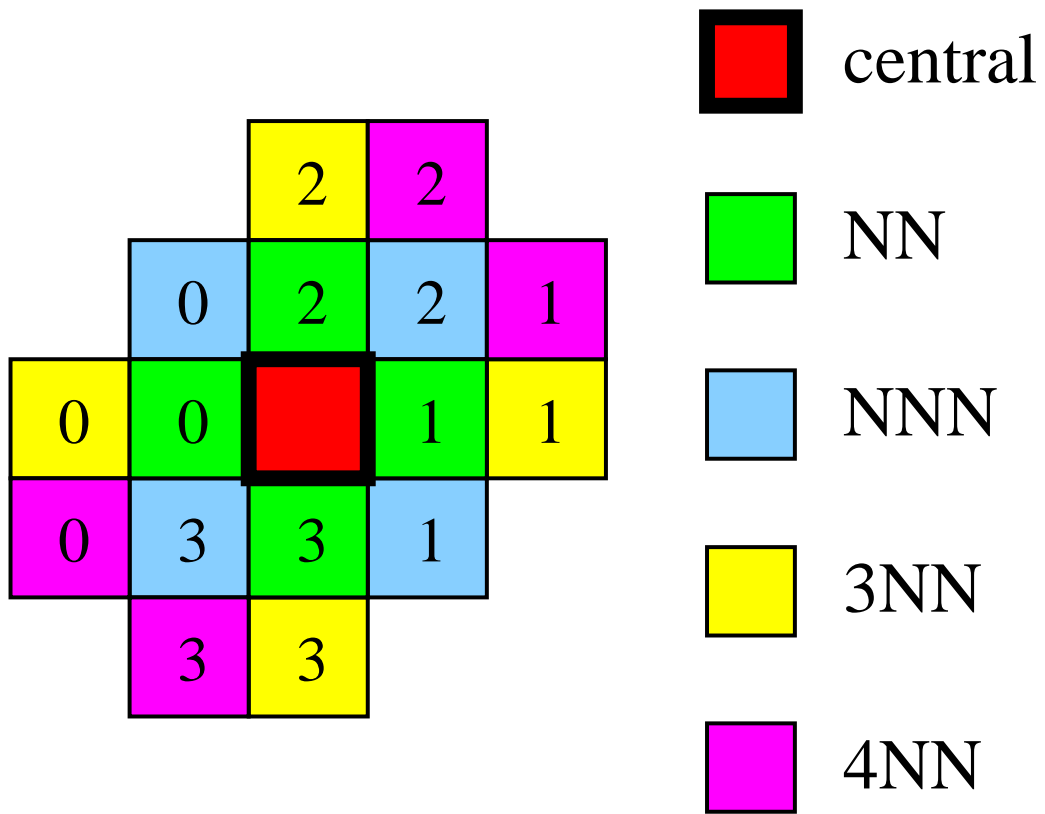


Fig. A-2. (color)